

REPORT DOCUMENTATION PAGE			Form Approved OMB NO. 0704-0188	
Public reporting burden for this collection of information is estimated to average 1 hour per response, including the time for reviewing instructions, searching existing data sources, gathering and maintaining the data needed, and completing and reviewing the collection of information. Send comment regarding this burden estimate or any other aspect of this collection of information, including suggestions for reducing this burden, to Washington Headquarters Services, Directorate for Information Operations and Reports, 1215 Jefferson Davis Highway, Suite 1204, Arlington, VA 22202-4302, and to the Office of Management and Budget, Paperwork Reduction Project (0704-0188), Washington, DC 20503.				
1. AGENCY USE ONLY (Leave blank)		2. REPORT DATE 12/28/97		3. REPORT TYPE AND DATES COVERED Final Report October 1994-September 1997
4. TITLE AND SUBTITLE Quantum Mechanical Balance Equation Approach to Semiconductor Device Modeling			5. FUNDING NUMBERS DAAH04-94-G-0413	
6. AUTHOR(S) Hong-Liang Cui				
7. PERFORMING ORGANIZATION NAMES(S) AND ADDRESS(ES) Stevens Institute of Technology Hoboken, New Jersey, 07030			8. PERFORMING ORGANIZATION REPORT NUMBER	
9. SPONSORING / MONITORING AGENCY NAME(S) AND ADDRESS(ES) U.S. Army Research Office P.O. Box 12211 Research Triangle Park, NC 27709-2211			10. SPONSORING / MONITORING AGENCY REPORT NUMBER ARO 33854.8-AL	
11. SUPPLEMENTARY NOTES The views, opinions and/or findings contained in this report are those of the author(s) and should not be construed as an official Department of the Army position, policy or decision, unless so designated by other documentation.				
12a. DISTRIBUTION / AVAILABILITY STATEMENT Approved for public release; distribution unlimited.			12 b. DISTRIBUTION CODE	
13. ABSTRACT (Maximum 200 words) This research project was focused on the development of a quantum mechanical balance equation based device simulator that can model advanced, compound, submicron devices, under all transport conditions (AC, DC, and transient response). This report documents the complete project, its planning, execution, and completion. The device models are described, along with representative simulation results for various devices, such as Si-MESFET, Si-MOSFET and GaAs-MESFET.				
19980519 097				
DTIC QUALITY INSPECTED 8				
14. SUBJECT TERMS			15. NUMBER OF PAGES	
			16. PRICE CODE	
17. SECURITY CLASSIFICATION OR REPORT UNCLASSIFIED			18. SECURITY CLASSIFICATION OF THIS PAGE UNCLASSIFIED	
19. SECURITY CLASSIFICATION OF ABSTRACT UNCLASSIFIED			20. LIMITATION OF ABSTRACT UL	

**Quantum Mechanical Balance Equation Approach
To Semiconductor Device Simulation**

Final Report

Submitted to

The U.S. Army Research Office

By

Stevens Institute of Technology

Principal Investigator:

Hong-Liang Cui

Department of Physics and Engineering Physics

Performance Period:

October 1, 1994 – September 30, 1997

Contract Number: DAAH04-94-G-0413

28 December 1997

1. Introduction

It is becoming increasingly important to use computer-aided device simulators in the design and fabrication processes of semiconductor devices designing as semiconductor devices continue to decrease in size toward the deep submicron regime. The development of devices involves several iterations of trial and error in fabrication until a specified goal in terms of design conditions is reached. The application of device modeling can provide an inexpensive way to analyze and design the semiconductor devices before expensive device processing. Since traditional equivalent circuit models and close-form analytical models cannot always provide consistently accurate results for all modes of operation of today's small devices. This has meant that there has been a greater demand for models capable of increasing our understanding of how these devices operate and capable of predicting accurate quantitative results.

To simulate a device, we solve a transport equation coupled with Poisson equation. The accuracy of a simulation is usually determined by how accurately carrier transport is described. Generally, the more sophisticated the approach, the heavier the computational burden, so it is important to choose an adequate approach for the device under study. In the past, the study of electric behavior in a semiconductor device has been based on the drift-diffusion equation. The drift-diffusion model is a low-order approximation of the Boltzmann transport equation, it implies that mobility of the carrier is only a function of the local electrical field and it does not take account of the non-stationary characteristics such as carrier heating and velocity overshoot [1,2]. The application of this model is limited to devices where the spatial variation of the electric field is not very large. However, in modern devices, whose size is in the deep submicron region, the non-stationary phenomena are becoming more important. As a result, the drift-diffusion model is no longer applicable [3-6].

Monte Carlo simulation has been widely used for analyzing carrier transport in bulk semiconductors [7,8,9]. This method tracks the momentum and position of an ensemble of carriers as they move through a device under the influence of an electric field and random scattering forces. Random numbers are chosen to determine the time between collisions, the type of scattering events encountered, and the direction of the carrier after scattering. Monte Carlo solution of the Boltzmann transport Equation can provide a more detailed description of carrier transport. This is because band structure and various scattering mechanisms can be taken into consideration [10,11]. However, the noise in the solution and the enormous amounts of computation time required make this model impractical for device design.

Another device simulation method is based on the hydrodynamic model, which is obtained by taking the first three moments of the Boltzmann Transport Equation [12-15]. These are the carrier continuity equation, the momentum balance equation, and the energy balance equation. Instead of solving for the carrier distribution function, the quantities of interest are calculated directly through the hydrodynamic equations. The hydrodynamic model has many advantages over the drift-diffusion model, such as its ability to treat high-field, nonstationary, and hot-electron effects. It can also model multi-dimensional devices without the excessive computational cost of the Monte Carlo

simulations. But it has been known to give unphysical solutions in some cases, e.g., the spurious velocity overshoot spike in $n^+ - n - n^+$ 'ballistic' diode [16]. The moments equations by themselves do not form a closed set of equations. The momentum and energy relaxation times are needed and can only be imported from outside of the system. These relaxation times are supplied from Monte Carlo simulations or simply assumed to be constant [17,18].

Recently, a hydrodynamic-balance-equations model of carrier transport in semiconductor devices based on the Lei-Ting balance equations has been developed [19,20,21]. The Lei-Ting balance equations have been successfully applied to many types of semiconductor microstructures, including studies of nonequilibrium phonon, nonstationary and high frequency transport [22,23]. Unlike other hydrodynamic equation based approaches to device modeling, where the various relaxation rates are imported from Monte Carlo calculations or simply assumed to be constant [24,25,26], the Lei-Ting hydrodynamic balance equations approach includes scattering in the form of frictional force functions due to electron-impurity and electron-phonon interaction and an energy loss function due to electron-phonon interaction. These quantities are calculated within the simulation process itself, as functions of the electron drift velocity, electron temperature, as well as the electron density, without an outside, separate Monte Carlo procedure [21,27,28]. Thus, besides the usual advantages of traditional hydrodynamic simulation approaches, the present method enjoys the added convenience of self-contained treatment of scattering.

This document reports on a systematic implementation of the Lei-Ting hydrodynamic balance equations as a sophisticated, versatile device simulation package, capable of 1D, 2D device modeling tasks encountered by device designers today. In addition to steady-state modeling, transient device simulations based on the new hydrodynamic model are also described. Without any complicated mathematics, a decoupled method with a relatively large time step has been applied to the transient simulation. The time discretization algorithm for our transient simulator is based on the Crank-Nicolson method for time discretization, and for the algorithm of the time step selection we use the local error to determine the size of each time step.

This report is organized as follows. In chapter 2, we give a brief review of the commonly used models of semiconductor transport, such as Monte Carlo method, drift-diffusion model and hydrodynamic model. A nonparabolic multivalley Lei-Ting balance equation is given in Chapter 3. Hydrodynamic balance equations for a single valley semiconductor have been described in Chapter 4. In Chapter 5, the discretization of the hydrodynamic balance equations is performed. The Box Integration Method is used for spatial discretization and the Crank-Nicolson implicit scheme is used for time discretization. In Chapter 6, we present some simulation results of the application of our hydrodynamic model. Discussion and conclusion are given in Chapter 7.

2. Models of Semiconductor Transport

2.1 Boltzmann Transport Equation and Monte Carlo Method

To simulate carrier motion in a submicron semiconductor device, one has to solve the Boltzmann transport equation and the Poisson equation simultaneously. The Boltzmann transport equation is given by:

$$\frac{\partial f}{\partial t} + \bar{v} \cdot \nabla_{\bar{r}} f + \frac{\bar{F}}{\hbar} \cdot \nabla_{\bar{k}} f = \left(\frac{\partial f}{\partial t} \right)_c, \quad (2.1)$$

where $f = f(\bar{r}, \bar{k}, t)$ is the distribution function, t is the time variable, \bar{v} is the carriers velocity, \bar{F} is the force on the carriers. The collision term on the right-hand side of equation (1) includes all the scattering mechanisms, and it is given by

$$\left(\frac{\partial f}{\partial t} \right)_c = \int [W(\bar{k}', \bar{k}) f_{\bar{k}'} (1 - f_{\bar{k}}) - W(\bar{k}, \bar{k}') f_{\bar{k}} (1 - f_{\bar{k}'})] dV_{\bar{k}'}. \quad (2.2)$$

Here, $W(\bar{k}, \bar{k}')$ is the transition probability, and $W(\bar{k}, \bar{k}') dV_{\bar{k}'} dt$ is the conditional probability of the transition from the state \bar{k}' in $dV_{\bar{k}'}$ in time dt given the an electron is initially in state \bar{k} and the state \bar{k}' is empty. A direct solution to the Boltzmann transport equation coupled to a self-consistent electric field pattern for any realistic semiconductor devices is rather difficult because the equation to be solved is a very complicated integro-differential equation with seven independent variables.

The most popular technique for solving the Boltzmann transport equation is the Monte Carlo method. This method tracks the position and momentum of an ensemble of particles as they move through a device under the influence of the electric field and random scattering forces. Random numbers are chosen to determine the time between collisions, the type of scattering events encountered, and the direction of the carrier after scattering. The process is repeated, typically between 10^4 and 10^6 times, to simulate the carrier path through the device. For the time dependent problems, the sample ensemble must be sufficiently large to accurately represent the actual electron gas.

The Monte Carlo simulation can provides more accurate simulations of carrier transport in a semiconductor device, it does have some limitations that should be mentioned. First, the intensive computer time required and the statistical noise associated with it limit this method's application. Although the statistical noise decreases as the number of simulated carriers, N_{sim} , increases, but it only drops as $\sqrt{N_{sim}}$, so unreasonably large number of carriers would have to be simulated. Second, Monte Carlo method is not well suited for dealing with the low-field region, barrier region and carrier generation-recombination processes.

2.2 The Drift-Diffusion model

Currently, most device modeling packages are based on the drift-diffusion (DD) model, which consists of the basic semiconductor equations

$$\frac{\partial n}{\partial t} - \frac{1}{e} \nabla \cdot (\bar{J}_n) = -U, \quad (2.3)$$

$$\nabla \cdot (\epsilon \nabla \phi) = e(N_D - n), \quad (2.4)$$

where

$$\bar{J}_n = eD_n \nabla n - en\mu_n \nabla \phi. \quad (2.5)$$

Equation (2.3) is the carrier-continuity equation, and (2.4) is the Poisson equation. Here, \bar{J}_n is the electron current density, n is the electron density, μ_n is the electron mobility, U is the net recombination rate per unit volume, ϕ is the electrical potential, and N_D is the donor density. Diffusivity and mobility are assumed to be related by the Einstein relation

$$D_n = \frac{k_B T}{e} \mu_n, \quad (2.6)$$

where T is the lattice temperature. The mobility is related to the momentum relaxation time and effective mass as follows:

$$\mu_n = \frac{e\tau_n}{m_n}. \quad (2.7)$$

Here τ_n and m_n are momentum relaxation time and effective mass of electron.

The drift-diffusion model can be shown to arise from the second-moment approximation to the Boltzmann transport equation. Since the drift-diffusion model are based on the assumptions that carriers are in local equilibrium with the lattice, and the mobility is a function of the local electric field, the applicability of this model is limited to devices where the spatial variation of the electric field is not very large. Due to rapid variations of the electric field in today's device, these assumptions are not always valid, and hence the transport coefficients cannot be considered to be dependent only on the local electrical field. The drift-diffusion model fails to predict phenomena such as carrier heating and velocity overshoot. Velocity overshoot can be explained if we recognize that the mobility is more closely related to the local carrier energy than the local electric field. Velocity overshoot occurs because at the beginning of the high field region the mobility is at its low field value. As the carrier energy rises, the mobility drops until the saturated velocity is reached. Velocity overshoot is a non-local effect and also is referred to as an off-equilibrium effect, because carriers do not have an opportunity to establish equilibrium with the local electric field in submicron devices. Velocity overshoot can improve the performance of small device because the average carrier velocity can exceed the steady state limit.

2.3 The Hydrodynamic model

The hydrodynamic model consists of a set of equations expressing the conservation of charge, momentum and energy for each species of carriers [4]. These equations are derived by taking the first three moments of the Boltzmann transport equation. The hydrodynamic equations for electrons can be written as follows:

$$\frac{\partial n}{\partial t} - \frac{1}{e} \nabla \cdot (\bar{J}_n) = -U, \quad (2.8)$$

$$\bar{J}_n + n\tau_{pn} \frac{d}{dt} \left(\frac{\bar{J}_n}{n} \right) = eD_n \nabla n + en\mu_n \left(\frac{k_B}{e} \nabla T_e - \nabla \phi \right), \quad (2.9)$$

$$\frac{\partial(nw_n)}{\partial t} + \nabla \cdot \bar{S}_n = \bar{J}_n \cdot \bar{E} - Uw_n + n \left(\frac{\partial w_n}{\partial t} \right)_c, \quad (2.10)$$

$$\nabla \cdot (\epsilon \nabla \phi) = e(N_D - n), \quad (2.11)$$

where T_e is the electron temperature, τ_{pn} is the electron momentum relaxation time, w_n is the electron mean energy, $\bar{E} = -\nabla \phi$ is the electric field. Here, the diffusion coefficient is given by the generalized Einstein relation

$$D_n = \frac{k_B T_e}{e} \mu_n, \quad (2.12)$$

where T_e is the electron temperature.

The electron energy flow \bar{S}_n is given by

$$\bar{S}_n = -\kappa_n \nabla T_e - (w_n + k_B T_e). \quad (2.13)$$

The thermal conductivity κ_n is related to the mobility μ_n by the Wiedmann-Franz law:

$$\kappa_n = \left(\frac{5}{2} + c \right) en\mu_n \left(\frac{k_B}{e} \right)^2 T_e, \quad (2.14)$$

where c is an adjustable parameter, usually taken to be -1 .

The electron mean energy w_n is defined as

$$w_n = \frac{3}{2} k_B T_e + \frac{1}{2} m_n v_n^2, \quad (2.15)$$

m_n the electron effective mass, and v_n the mean velocity of electron.

The collision terms are modeled by the relaxation-time approximation. The collision term in (2.10) is expressed as:

$$\left(\frac{\partial w_n}{\partial t} \right)_c = - \frac{w_n - w_0}{\tau_{wn}}, \quad (2.16)$$

where τ_{wn} is the energy relaxation time for the electron.

Two parameters are needed in applying the hydrodynamic model: the momentum relaxation time and the energy relaxation time. A common approach is to extract these parameters from bulk homogeneous Monte Carlo simulations. An alternative method is to use various empirical mobility models, such as [29]:

$$\mu_n = \frac{\mu_0}{1 + \gamma(w - w_0)}; \quad \gamma = \frac{\mu_0}{e\tau_{w0}v_{sat}^2}, \quad (2.17)$$

where v_{sat} is the electron saturation velocity, μ_0 is the low-field mobility, and τ_{w0} is the low-field energy relaxation time in the homogeneous case.

Although hydrodynamic models include more physics than does the drift-diffusion model, serious errors may occur in practice, e.g., the spurious velocity overshoot spike in $n^+ - n - n^+$ 'ballistic' diode. This spurious peak can be eliminated by varying the value of the thermal conductivity in the Wiedmann-Franz law. However, the value of the

thermal conductivity depends on the doping distribution and on the applied voltages, therefore it has to be adjusted to fit the individual devices.

3. The Lei-Ting Hydrodynamic Balance Equations for a Nonparabolic Multivalley Semiconductor

The Lei-Ting balance equation approach for hot electron transport in semiconductors is based on the Heisenberg equations of motion for the total physical momentum, the total energy and the population of carriers in each energy valley, and the statistical average with respect to an initial density matrix having a lattice wave-vector shift, an electron temperature, and a chemical potential for each energy valley as parameters.

Here, we consider a semiconductor system with an n -valley band structure in a electric field \vec{E} and the energy band $\varepsilon_a(\vec{k})$ has a general spectrum functions in the \vec{k} space. The equations for momentum, energy and carrier numbers balance in the a th valley are written in the form [30]:

$$\begin{aligned} \frac{d}{dt}(N_a \bar{v}_a) = N_a e \vec{E} \cdot \mathbf{K}_a + \bar{A}_{ei}^a + \bar{A}_{ep}^a \\ + \sum_{b(\neq a)} \bar{A}_{ei}^{ab} + \sum_{b(\neq a)} \bar{A}_{ep}^{ab} + \sum_{b(\neq a)} \bar{A}_{ee}^{ab}, \end{aligned} \quad (3.1)$$

$$\frac{d}{dt}(N_a \varepsilon_a) = N_a e \vec{E} \cdot \bar{v}_a - W_{ep}^a - \sum_{b(\neq a)} W_{ep}^{ab} - \sum_{b(\neq a)} W_{ee}^{ab}, \quad (3.2)$$

$$\frac{d}{dt} N_a = \sum_{b(\neq a)} X_{ei}^{ab} + \sum_{b(\neq a)} X_{ep}^{ab}. \quad (3.3)$$

Here, N_a is the average number, \bar{v}_a is the average velocity, ε_a is the average energy, \mathbf{K}_a is the ensemble-averaged inverse effective mass tensor, \bar{A}^a is the frictional acceleration contributed from the intravalley scattering, \bar{A}^{ab} is the frictional acceleration contributed from the intervalley scattering, \bar{A}_{ee}^{aa} is the frictional acceleration contributed from the electron intravalley-intravalley Coulomb scattering, W_{ep}^a is the energy loss rate due to the intravalley electron-phonon scattering, W_{ep}^{ab} is the energy loss rate due to the intervalley scattering, W_{ee}^{ab} is the energy loss rate due to the electron intravalley-intravalley Coulomb scattering, and X^{ab} is the rate of numbers change of the carriers in the a th energy valley. The statistic averages of the relevant quantities are defined by the following

$$N_a = 2 \sum_{\vec{k}} f[(\varepsilon_a(\vec{k}) - \mu_a) / T_a], \quad (3.4)$$

$$\bar{v}_a = \frac{2}{N_a} \sum_{\vec{k}} \bar{v}_a(\vec{k}) f[(\bar{\varepsilon}_a(\vec{k}) - \mu_a) / T_a], \quad (3.5)$$

$$\varepsilon_a = \frac{2}{N_a} \sum_{\vec{k}} \varepsilon_a(\vec{k}) f[(\bar{\varepsilon}_a(\vec{k}) - \mu_a) / T_a], \quad (3.6)$$

$$\mathbf{K}_a = \frac{2}{N_a} \sum_{\vec{k}} [\nabla_{\vec{k}} \nabla_{\vec{k}} \varepsilon_a(\vec{k})] f[(\bar{\varepsilon}_a(\vec{k}) - \mu_a) / T_a], \quad (3.7)$$

$$\bar{\varepsilon}_a(\vec{k}) \equiv \varepsilon_a(\vec{k} - \vec{p}_a), \quad (3.8)$$

where $f(x) \equiv 1/[\exp(x)+1]$ is the Fermi-Dirac function, \bar{p}_a is the average lattice momentum, μ_a is the chemical potential, T_a is the carrier temperature, and the velocity function of carriers \bar{v}_a is given by

$$\bar{v}_a(\vec{k}) = \nabla_{\vec{k}} \varepsilon_a(\vec{k}). \quad (3.9)$$

The average drift velocity of the whole system is given by

$$\bar{v}_d = N^{-1} \sum_a N_a \bar{v}_a, \quad (3.10)$$

where N is the total carrier number in this system.

The intravalley frictional acceleration due to the electron-impurity scattering is given by

$$\begin{aligned} \bar{A}_{ei}^a = & -2\pi n_i \sum_{\vec{k}, \vec{q}} |u(\vec{q})|^2 |g_{aa}(\vec{k}, \vec{q})|^2 [\bar{v}_a(\vec{k}) - \bar{v}_a(\vec{k} + \vec{q})] \delta[\varepsilon_a(\vec{k}) - \varepsilon_a(\vec{k} + \vec{q})] \\ & \times \frac{f(\bar{\varepsilon}_a(\vec{k}), T_a) - f(\bar{\varepsilon}_a(\vec{k} + \vec{q}), T_a)}{|\epsilon_a^{RPA}[\vec{q}, \bar{\varepsilon}_a(\vec{k}) - \bar{\varepsilon}_a(\vec{k} + \vec{q})]|^2}, \end{aligned} \quad (3.11)$$

and the intravalley frictional acceleration due to the electron-phonon scattering is given by

$$\begin{aligned} \bar{A}_{ep}^a = & -4\pi \sum_{\vec{k}, \vec{q}} |M(\vec{q})|^2 |g_{aa}(\vec{k}, \vec{q})|^2 [\bar{v}_a(\vec{k}) - \bar{v}_a(\vec{k} + \vec{q})] \delta[\varepsilon_a(\vec{k}) - \varepsilon_a(\vec{k} + \vec{q})] \\ & \times \frac{f(\bar{\varepsilon}_a(\vec{k}), T_a) - f(\bar{\varepsilon}_a(\vec{k} + \vec{q}), T_a)}{|\epsilon_a^{RPA}[\vec{q}, \bar{\varepsilon}_a(\vec{k}) - \bar{\varepsilon}_a(\vec{k} + \vec{q})]|^2} \left[n \left(\frac{\hbar \Omega_{\vec{q}\lambda}}{k_B T} \right) - n \left(\frac{\bar{\varepsilon}_a(\vec{k}) - \bar{\varepsilon}_a(\vec{k} + \vec{q})}{k_B T_a} \right) \right]. \end{aligned} \quad (3.12)$$

The energy loss rate contributed from the intravalley scattering is expressed as

$$\begin{aligned} W_{ep}^a = & 4\pi \sum_{\vec{k}, \vec{q}, \lambda} |M(\vec{q}, \lambda)|^2 |g_{aa}(\vec{k}, \vec{q})|^2 \Omega_{\vec{q}, \lambda} \delta[\varepsilon_a(\vec{k}) - \varepsilon_a(\vec{k} + \vec{q}) - \hbar \Omega_{\vec{q}\lambda}] \\ & \times \frac{f(\bar{\varepsilon}_a(\vec{k}), T_a) - f(\bar{\varepsilon}_a(\vec{k} + \vec{q}), T_a)}{|\epsilon_a^{RPA}[\vec{q}, \bar{\varepsilon}_a(\vec{k}) - \bar{\varepsilon}_a(\vec{k} + \vec{q})]|^2} \left[n \left(\frac{\hbar \Omega_{\vec{q}\lambda}}{k_B T} \right) - n \left(\frac{\bar{\varepsilon}_a(\vec{k}) - \bar{\varepsilon}_a(\vec{k} + \vec{q})}{k_B T_a} \right) \right]. \end{aligned} \quad (3.13)$$

The intervalley frictional acceleration due to the electron-impurity scattering \bar{A}_{ei}^{ab} is given by

$$\begin{aligned} \bar{A}_{ei}^{ab} = & -2\pi n_i \sum_{\vec{k}, \vec{q}} |u(\vec{q})|^2 |g_{ab}(\vec{k}, \vec{q})|^2 \bar{v}_a(\vec{k}) \delta[\varepsilon_a(\vec{k}) - \varepsilon_b(\vec{k} + \vec{q})] \\ & \times [f(\bar{\varepsilon}_a(\vec{k}), T_a) - f(\bar{\varepsilon}_b(\vec{k} + \vec{q}), T_b)]. \end{aligned} \quad (3.14)$$

And the intervalley frictional acceleration due to electron-phonon scattering \bar{A}_{ep}^{ab} is given by

$$\bar{A}_{ep}^{ab} = -4\pi \sum_{\vec{k}, \vec{q}, \lambda} |M(\vec{q}, \lambda)|^2 |g_{ab}(\vec{k}, \vec{q})|^2 \bar{v}_a(\vec{k}) \Lambda_+^{ab}(\vec{k}, \vec{q}, \Omega_{\vec{q}\lambda}). \quad (3.15)$$

The frictional acceleration contributed from the electron intravalley Coulomb scattering \bar{A}_{ee}^{ab} is given by

$$\bar{A}_{ee}^{ab} = -2 \sum_{\vec{k}, \vec{k}', \vec{q}} |v_c(\vec{q})|^2 |g_{aa}(\vec{k}, \vec{q})|^2 |g_{bb}(\vec{k}', \vec{q})|^2 [\bar{v}_a(\vec{k}) - \bar{v}_a(\vec{k} + \vec{q})] Y^{ab}(\vec{k}, \vec{k}', \vec{q}). \quad (3.16)$$

The energy-loss rate due to the intervalley electron-phonon scattering is expressed as

$$W_{ep}^{ab} = -4\pi \sum_{\vec{k}, \vec{q}, \lambda} |M(\vec{q}, \lambda)|^2 |g_{ab}(\vec{k}, \vec{q})|^2 \varepsilon_a(\vec{k}) \Lambda_+^{ab}(\vec{k}, \vec{q}, \Omega_{\vec{q}\lambda}), \quad (3.17)$$

and the intravalley Coulomb scattering energy-loss rate is given by

$$W_{ee}^{ab} = -2 \sum_{\vec{k}, \vec{k}', \vec{q}} |v_c(\vec{q})|^2 |g_{aa}(\vec{k}, \vec{q})|^2 |g_{bb}(\vec{k}', \vec{q})|^2 [\varepsilon_a(\vec{k}) - \varepsilon_a(\vec{k} + \vec{q})] Y^{ab}(\vec{k}, \vec{k}', \vec{q}) \quad (3.18)$$

The rate of numbers change of the carriers in the a th energy valley due to the electron-impurity scattering is given by

$$X_{ei}^{ab} = -2\pi n_i \sum_{\vec{k}, \vec{q}} |u(\vec{q})|^2 |g_{ab}(\vec{k}, \vec{q})|^2 \delta[\varepsilon_a(\vec{k}) - \varepsilon_b(\vec{k} + \vec{q})] [f(\bar{\varepsilon}_a(\vec{k}), T_a) - f(\bar{\varepsilon}_b(\vec{k} + \vec{q}), T_b)], \quad (3.19)$$

and the rate of numbers change of carriers due to the electron-phonon scattering is given by

$$X_{ep}^{ab} = -4\pi \sum_{\vec{k}, \vec{q}, \lambda} |M(\vec{q}, \lambda)|^2 |g_{ab}(\vec{k}, \vec{q})|^2 \Lambda_+^{ab}(\vec{k}, \vec{q}, \Omega_{\vec{q}\lambda}). \quad (3.20)$$

Here,

$$\begin{aligned} \Lambda_+^{ab} = & [f(\bar{\varepsilon}_a(\vec{k}), T_a) - f(\bar{\varepsilon}_b(\vec{k} + \vec{q}), T_b)] \left[n \left(\frac{\hbar \Omega_{\vec{q}\lambda}}{k_B T} \right) - n \left(\frac{\bar{\varepsilon}_a(\vec{k})}{k_B T_a} - \frac{\bar{\varepsilon}_b(\vec{k} + \vec{q})}{k_B T_b} \right) \right] \delta[\varepsilon_a(\vec{k}) - \varepsilon_b(\vec{k} + \vec{q}) - \hbar \Omega_{\vec{q}\lambda}] \\ & + [f(\bar{\varepsilon}_a(\vec{k}), T_a) - f(\bar{\varepsilon}_b(\vec{k} + \vec{q}), T_b)] \left[n \left(\frac{\hbar \Omega_{\vec{q}\lambda}}{k_B T} \right) - n \left(\frac{\bar{\varepsilon}_b(\vec{k} + \vec{q})}{k_B T_b} - \frac{\bar{\varepsilon}_a(\vec{k})}{k_B T_a} \right) \right] \delta[\varepsilon_a(\vec{k}) - \varepsilon_b(\vec{k} + \vec{q}) + \hbar \Omega_{\vec{q}\lambda}], \end{aligned} \quad (3.21)$$

and

$$\begin{aligned} Y^{ab}(\vec{k}, \vec{k}', \Omega) = & 2\pi \delta[\varepsilon_a(\vec{k}) - \varepsilon_a(\vec{k} + \vec{q}) + \varepsilon_b(\vec{k}' + \vec{q}) - \varepsilon_b(\vec{k}')] \\ & \times \left| \epsilon_a^{\text{RPA}}[\vec{q}, \bar{\varepsilon}_a(\vec{k}) - \bar{\varepsilon}_a(\vec{k} + \vec{q})] \right|^{-2} \left| \epsilon_b^{\text{RPA}}[\vec{q}, \bar{\varepsilon}_b(\vec{k}') - \bar{\varepsilon}_b(\vec{k}' + \vec{q})] \right|^{-2} \\ & \times [f(\bar{\varepsilon}_a(\vec{k}), T_a) - f(\bar{\varepsilon}_a(\vec{k} + \vec{q}), T_a)] [f(\bar{\varepsilon}_b(\vec{k}'), T_b) - f(\bar{\varepsilon}_b(\vec{k}' + \vec{q}), T_b)] \\ & \times \left[n \left(\frac{\bar{\varepsilon}_a(\vec{k}) - \bar{\varepsilon}_a(\vec{k} + \vec{q})}{k_B T_a} \right) - n \left(\frac{\bar{\varepsilon}_b(\vec{k}') - \bar{\varepsilon}_b(\vec{k}' + \vec{q})}{k_B T_b} \right) \right]. \end{aligned} \quad (3.22)$$

and the Bose distribution function is expressed as

$$n(x) = \frac{1}{\exp(x) - 1}. \quad (3.23)$$

In the above equations, n_i is the impurity density, $\Omega_{\vec{q}\lambda}$ is the phonon frequency of the λ th branch with wave vector \vec{q} , the intravalley, $u(\vec{q})$ is the electron-impurity potential, $M(\vec{q}, \lambda)$ is the electron-phonon matrix element, $v_c(\vec{q})$ is the electron-electron Coulomb potential in the plane-wave representation, and $g_{aa}(\vec{k}, \vec{q})$ and $g_{ab}(\vec{k}, \vec{q})$ are, respectively, the intravalley and intervalley form factors related to the wave functions of the a th and b th energy valley,

$$|g(\vec{k}, \vec{q})|^2 = (a_{\vec{k}} a_{\vec{k} + \vec{q}} + c_{\vec{k}} c_{\vec{k} + \vec{q}} \cos \theta)^2, \quad (3.24)$$

with

$$a_{\vec{k}} = \left[\frac{1 + \alpha \varepsilon(\vec{k})}{1 + 2\alpha \varepsilon(\vec{k})} \right]^{1/2}, \quad c_{\vec{k}} = \left[\frac{\alpha \varepsilon(\vec{k})}{1 + 2\alpha \varepsilon(\vec{k})} \right]^{1/2}. \quad (3.25)$$

For intravalley scattering, we consider the intravalley carrier screening in the random-phase approximation (RPA), $\epsilon_a^{\text{RPA}}(\vec{q}, \omega)$ is the RPA dielectric function of the a th valley.

For a Kane-type nonparabolic energy band, the relationship between the energy and the wave vector can be written as

$$\epsilon_a(\vec{k}) = \frac{1}{2\alpha} \left[\sqrt{1 + 4\alpha \epsilon_a^{(p)}(\vec{k})} - 1 \right], \quad (3.26)$$

where α is the nonparabolic parameter. The parabolic energy dispersion of the a th valley is given by

$$\epsilon_a^{(p)}(\vec{k}) = \frac{(k_x - k_{ax})^2}{2m_{ax}} + \frac{(k_y - k_{ay})^2}{2m_{ay}} + \frac{(k_z - k_{az})^2}{2m_{az}}, \quad (3.27)$$

where $1/m_{ax}$, $1/m_{ay}$, and $1/m_{az}$ are the x , y , and z components of the inverse effective mass tensor, respectively, and \vec{k}_a indicates the position in the Brillouin zone of the center of the a th valley.

The scattering mechanisms which have been considered may include intravalley electron-impurity scattering, intravalley electron-phonon scattering (acoustic and optic), intervalley electron-phonon scattering (acoustic and optic), and electron-electron interaction.

For Si, the electrons which contribute to transport are those in the six equivalent valleys which lie along the $\langle 100 \rangle$ directions, as shown in Fig 3.1.

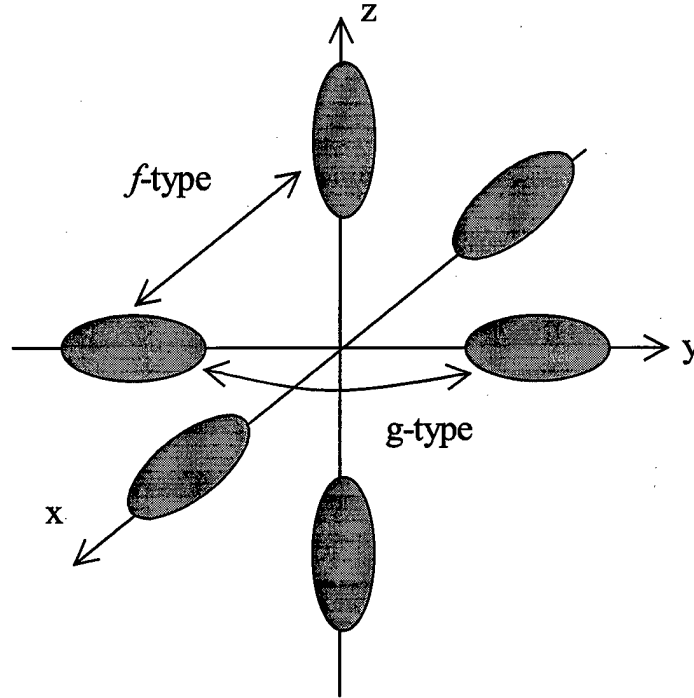


Fig. 3.1 Constant energy surfaces for the conduction band of silicon.

There are two types of intervalley scattering in Si: g -type (between parallel valleys) and f -type (between perpendicular valleys). So that, the squared matrix elements for g -type and f -type scatterings are represented by

$$|M_{ab}|^2 = \frac{\hbar D_{g\lambda}^2}{2\Omega_{g\lambda} d} \quad (\text{for } a=1, b=2), \quad (3.28)$$

and

$$|M_{ab}|^2 = \frac{\hbar D_{f\lambda}^2}{2\Omega_{f\lambda} d} \quad (\text{for } a=1, b=3,4,5,6). \quad (3.29)$$

For the acoustic intravalley scattering, the squared matrix elements is given by

$$|M_{aa}|^2 = \frac{\hbar E_1^2 q}{2v_s d}. \quad (3.30)$$

Table 1. Physical parameters for Silicon[30].

Mass density	d	2.329 g/cm^3
Longitudinal sound velocity	v_s	$9.04 \times 10^5 \text{ cm/s}$
Longitudinal effective mass	m_l	$0.916 m_0$
Transverse effective mass	m_t	$0.19 m_0$
Dielectric constant	κ	11.7
Longitudinal optical phonon energy	$\hbar\omega_0$	0.063 eV
Acoustic deformation potential	E_1	9.2 eV
Nonparabolicity parameter	α	0.5 eV^{-1}
Intervalley scattering		
	Equivalent temperature (K)	Coupling constant ($\times 10^8 \text{ eV/cm}$)
<i>f</i> -type	$\Omega_{f\lambda}$	$D_{f\lambda}$
	210	0.15
	500	3.4
	600	4.0
<i>g</i> -type	$\Omega_{g\lambda}$	$D_{g\lambda}$
	140	0.5
	210	0.8
	700	3.0

4. Hydrodynamic Balance Equations for a Single Valley Semiconductor

4.1 Lei-Ting Balance Equation for a Single Parabolic Energy Band

The Lei-Ting balance equations for a single parabolic band system can be summarized as follows [19,21]:

$$\frac{\partial n}{\partial t} - \frac{1}{e} \nabla \cdot (\bar{J}) = -U, \quad (4.1)$$

$$\frac{\partial \bar{v}}{\partial t} + (\bar{v} \cdot \nabla) \bar{v} = -\frac{2}{3} \frac{\nabla u}{mn} + \frac{e}{m} \bar{E} + \frac{\bar{f}}{mn}, \quad (4.2)$$

$$\frac{\partial u}{\partial t} + \bar{v} \cdot \nabla u = -\frac{5}{3} u \nabla \cdot \bar{v} - W - \bar{v} \cdot \bar{f} - \nabla \cdot \bar{Q} \quad (4.3)$$

$$\nabla^2 \phi = -\frac{e}{\epsilon} (N_D - n), \quad (4.4)$$

where n is the statistical average of the electron number density, \bar{v} is the average velocity of the electrons, U is the net recombination rate per unit volume, u is the average kinetic energy of the relative electrons. The symbol \bar{f} denotes the frictional force experienced by the electrons due to impurity and phonon scattering, W is the energy-loss rate of the electron system to the phonon system, $\nabla \cdot \bar{Q}$ is the heat flow. The symbols e and m are the electron charge and effective mass, ϵ is the static background dielectric constant, N_D is the net doping concentration.

The average local kinetic energy density of the relative electrons is given by

$$u(\vec{R}) = 2 \sum_{\vec{k}} \epsilon_{\vec{k}} f_0[(\epsilon_{\vec{k}} - \mu(\vec{R}))/k_B T_e(\vec{R})] \quad (4.5)$$

The local chemical potential $\mu(\vec{R})$ is related to the local electron density $n(\vec{R})$ via the relation

$$n(\vec{R}) = 2 \sum_{\vec{k}} f_0[(\epsilon_{\vec{k}} - \mu(\vec{R}))/k_B T_e(\vec{R})] \quad (4.6)$$

where $\epsilon_{\vec{k}}$ is the band energy of the electron, and f_0 is the Fermi-Dirac function.

With the help of the Fermi integrals, the local carrier number and the internal energy densities can be expressed as

$$n = N_c(T_e) \mathcal{F}_{1/2}(\alpha_e), \quad (4.7)$$

$$u = \frac{3}{2} k_B T_e N_c(T_e) \mathcal{F}_{3/2}(\alpha_e), \quad (4.8)$$

where

$$\alpha_e = \frac{\mu}{k_B T_e}, \quad (4.9)$$

and the effective density of states in the conduction band N_c is

$$N_c = 2 \left(\frac{m k_B T_e}{2\pi\hbar^2} \right)^{3/2}. \quad (4.10)$$

The Fermi integral of order j is given by

$$\mathcal{F}_j(x) = \frac{1}{\Gamma(j+1)} \int_0^\infty dy \frac{y^j}{\exp(y-x)+1}. \quad (4.11)$$

At room temperature, the variable x in the Fermi integral (4.11) is much less than zero, so that the Fermi integral can be approximated by its nondegenerate form

$$\mathcal{F}_j(x) = \exp(x), \quad (4.12)$$

for not too high densities.

The resistive force is

$$\begin{aligned} \bar{f} = n_I \sum_{\bar{q}} |U(\bar{q})|^2 \bar{q} \Pi_2(\bar{q}, \omega_0) \\ + 2 \sum_{\bar{q}, \lambda} |M(\bar{q}, \lambda)|^2 \bar{q} \Pi_2(\bar{q}, \omega_0 + \Omega_{\bar{q}, \lambda}) \times \left\{ n_B \left(\frac{\hbar \Omega_{\bar{q}, \lambda}}{k_B T} \right) - n_B \left(\frac{\hbar(\omega_0 + \Omega_{\bar{q}, \lambda})}{k_B T_e} \right) \right\}, \end{aligned} \quad (4.13)$$

and the energy loss rate is

$$W = 2 \sum_{\bar{q}, \lambda} |M(\bar{q}, \lambda)|^2 \Omega_{\bar{q}, \lambda} \Pi_2(\bar{q}, \omega_0 + \Omega_{\bar{q}, \lambda}) \times \left\{ n_B \left(\frac{\hbar \Omega_{\bar{q}, \lambda}}{k_B T} \right) - n_B \left(\frac{\hbar(\omega_0 + \Omega_{\bar{q}, \lambda})}{k_B T_e} \right) \right\}, \quad (4.14)$$

where $\omega_0 = \bar{q} \cdot \bar{v}(\bar{R})$, $n_B(x) = (e^x - 1)^{-1}$ is the Bose-Einstein factor, n_I is impurity density, $\Omega_{\bar{q}, \lambda}$ is the phonon frequency of wave vector \bar{q} and branch index λ , $U(\bar{q})$ is the Fourier transform of the electron-impurity interaction potential, $M(\bar{q}, \lambda)$ is the electron-phonon coupling matrix element, $\Pi_2(\bar{q}, \omega)$ is the imaginary part of the density-density correlation function of electrons that can be obtained within the random-phase approximation (RPA) or beyond. Note that \bar{f} and W depend on the position vector \bar{R} through the quantities $n(\bar{R})$, $T_e(\bar{R})$, and $\bar{v}(\bar{R})$.

4.2 Scatting Mechanisms

The total resistive force density f is composed of two parts, due to impurity scattering and phonon scattering:

$$f = f_{imp} + f_{ph}, \quad (4.15)$$

which in the case of a three-dimensional bulk semiconductor are given as

$$f_{imp} = -\frac{n_I m^2 k_B T_e}{(2\pi)^3 \hbar^4} \int_{-1}^1 dx \int_0^\infty dq |q U(q)|^2 x P_2(q, \omega_0), \quad (4.16)$$

$$f_{ph} = -\frac{2m^2 k_B T_e}{(2\pi)^3 \hbar^4} \int_{-1}^1 dx \int_0^\infty dq \sum_{\lambda} |q M(q, \lambda)|^2 x P_2(q, \Omega_{q, \lambda} + \omega_0) \Delta n_B(\Omega_{q, \lambda}, \omega_0), \quad (4.17)$$

where $\omega_0 = qv_x$, and $(\beta_e = 1/k_B T_e)$,

$$\Delta n_B(\Omega_{q\lambda}, \omega) = n_B(\beta \hbar \Omega_{q\lambda}) - n_B(\beta \hbar (\Omega_{q\lambda} + \omega)). \quad (4.18)$$

The energy loss rate is determined by inelastic electron-phonon scattering

$$W = -\frac{2m^2 k_B T_e}{(2\pi)^3 \hbar^4} \int_{-1}^1 dx \int_0^\infty dq \sum_{q\lambda} q \Omega_{q\lambda} |M(q\lambda)|^2 P_2(q, \Omega_{q\lambda} + \omega_0) \Delta n_B(\Omega_{q\lambda}, \omega_0). \quad (4.19)$$

Usually, the resistive force densities and energy-loss rate are calculated based on the RPA density-density correlation function,

$$\Pi_2(q, \omega) = \frac{\Pi_2^{(0)}(q, \omega)}{1 - v_c(q) \Pi_2^{(0)}(q, \omega)}, \quad (4.20)$$

where $\Pi_2^{(0)} = -(m^2 k_B T_e / 2\pi \hbar^4 q) P_2$, and

$$P_2^{(0)}(q, \omega) = \ln \left(\frac{1 + \exp \left\{ -\frac{\beta \hbar^2}{2m} \left(\frac{q}{2} - \frac{m\omega}{\hbar q} \right)^2 + \alpha_e \right\}}{1 + \exp \left\{ -\frac{\beta \hbar^2}{2m} \left(\frac{q}{2} + \frac{m\omega}{\hbar q} \right)^2 + \alpha_e \right\}} \right), \quad (4.21)$$

is the noninteracting electron density-density correlation function, and $v_c(q) = e^2 / \epsilon q^2$ is the Fourier transform of the electron-electron Coulomb interaction potential.

The scattering of electrons by impurities such as ionized donors are described by the screened Coulomb potential, whose Fourier transform is given by

$$U(q) = \frac{e^2}{\epsilon(q^2 + q_D^2)}, \quad (4.22)$$

where q_D is the Debye wavevector

$$q_D^2 = \frac{e^2 n}{\epsilon k_B T_e} f_D, \quad (4.23)$$

with the temperature and density dependent factor f_D given by

$$f_D = \frac{\mathcal{F}_{-1/2}(\alpha_e)}{\mathcal{F}_{1/2}(\alpha_e)}. \quad (4.24)$$

The electron-phonon scattering includes acoustic phonons (with deformation potential coupling and piezoelectric coupling), optical phonons (polar and nonpolar), intervalley phonon scattering, as well as interface and confined phonon scattering. We consider only acoustic deformation coupling and nonpolar optic coupling in our example of a silicon device.

In the case of deformation potential for carrier acoustic-phonon interaction, only the longitudinal phonon contributes. The carrier-phonon matrix element takes the form

$$|M(q\lambda)|^2 = \frac{\hbar E_1^2 q^2}{2\Omega_q d}, \quad (4.25)$$

where d is the mass density of the lattice and E_1 is the deformation potential. For the dispersion relation of the longitudinal-acoustic phonon we use the Debye spectrum

$$\Omega_q = \Omega_s = v_s q, \quad (4.26)$$

with v_s denoting the sound speed for longitudinal waves. For the optic-phonon scattering, we take the optical mode frequency as a constant (the Einstein model):

$$\Omega_{q\lambda} = \Omega_0. \quad (4.27)$$

For the matrix element of electron-nonpolar optical-phonon interaction, we use

$$|M(q\lambda)|^2 = \frac{\hbar D^2}{2\Omega_0 d}, \quad (4.28)$$

where D is the shift of the band edge per unit relative displacement of the two sublattices relative to the optical mode.

4.3 Equivalence to the Conventional Hydrodynamic Equations

The Lei-Ting hydrodynamic balance equations can be shown to be equivalent to the hydrodynamic equations derived from Boltzmann equation [6]. The latter have the form

$$\nabla^2 \phi = -\frac{e}{\epsilon}(N_D - n), \quad (4.29)$$

$$\frac{\partial n}{\partial t} - \frac{1}{e} \nabla \cdot (\bar{J}_n) = -U, \quad (4.30)$$

$$\frac{\partial(nw_n)}{\partial t} + \nabla \cdot \bar{S} = \bar{J}_n \cdot \bar{E} - U w_n + n \left(\frac{\partial w_n}{\partial t} \right)_c, \quad (4.31)$$

$$\bar{J}_n - \frac{mnv}{ef} (\bar{J}_n \cdot \nabla) \left(\frac{\bar{J}_n}{n} \right) = \frac{enk_B T_e v}{f} \left(\nabla n + \frac{n}{T_e} \nabla T_e - \frac{en}{k_B T_e} \nabla \phi \right). \quad (4.32)$$

The energy flux density is

$$\bar{S}_n = \bar{Q} - \frac{\bar{J}_n}{e} \left(\frac{5u}{3n} + \frac{1}{2} m v^2 \right), \quad (4.33)$$

where $\bar{Q} = -\kappa_n \nabla T_e$ is the heat flux.

The average single particle energy is given by

$$w = \frac{1}{2} m v^2 + \frac{u}{n}, \quad (4.34)$$

and the energy relaxation rate is related to the rate of change of the particle number and the energy dissipation rate given by

$$\left(\frac{\partial w}{\partial t} \right)_c = -\frac{1}{n} \left\{ \frac{u}{n} \left(\frac{\partial n}{\partial t} \right)_c + W \right\}, \quad (4.35)$$

with

$$\left(\frac{\partial n}{\partial t} \right)_c = -U. \quad (4.36)$$

If the recombination-generation processes were not taken into account ($U = 0$), the energy relaxation rate reduces to

$$n \left(\frac{\partial w}{\partial t} \right)_c = -W. \quad (4.37)$$

The average carrier energy consists of the thermal energy $\frac{3}{2}k_B T_e$ and the kinetic energy $\frac{1}{2}m_n v^2$. But in this work we neglect the kinetic energy which is negligible compared with the thermal energy.

5. The Discretization of the Semiconductor Device Equations

The hydrodynamic balance equations consist of the Poisson and the three balance equations. These equations form a set of nonlinear, coupled, time-dependent partial differential equations. The solution methods can be divided into two categories: coupled (Newton) or decoupled (Gummel) method [31]. The use of the Newton method is limited by the requirement of proper choice of the initial guess. If the initial guess is far from the true solution, convergence is usually difficult to achieve. Furthermore, since the equations are solved simultaneously, CPU memory requirement of the Newton method is higher than that for a decouple method. In the decoupled method, the major variables are solved with currently available values iteratively. The advantages of decoupled method are simplicity, low memory requirements and convergence for arbitrary initial guesses. In our simulator, we use Gummel method to solve the hydrodynamic balance equations.

It is well known that the numerical solution of central difference scheme for the drift-diffusion equation exhibits oscillations if the grid is too coarse or if the drift velocity is too large relative to diffusion. Although these oscillations can be avoided by using sufficiently fine grids, it will cost too much computation time. This difficulty can be circumvented by introducing the Scharfetter-Gummel scheme or by using the artificial diffusivity. We chose the Scharfetter-Gummel scheme for the discretization of the flux continuity equations in this work. In the Scharfetter-Gummel scheme, a first-order ordinary differential equation is integrated by finding an integration factor. This approach results in an exponentially weighted difference scheme that prohibits the oscillations in the solution without requiring an excessive number of grid points.

5.1 The Box Integration Method

Device simulation requires numerical solution of partial differential equations. To solve the partial differential equations on a computer, they must be discretized on a simulation grid. The device is partitioned into a finite number of subdomains as illustrated in Fig. 5.1.

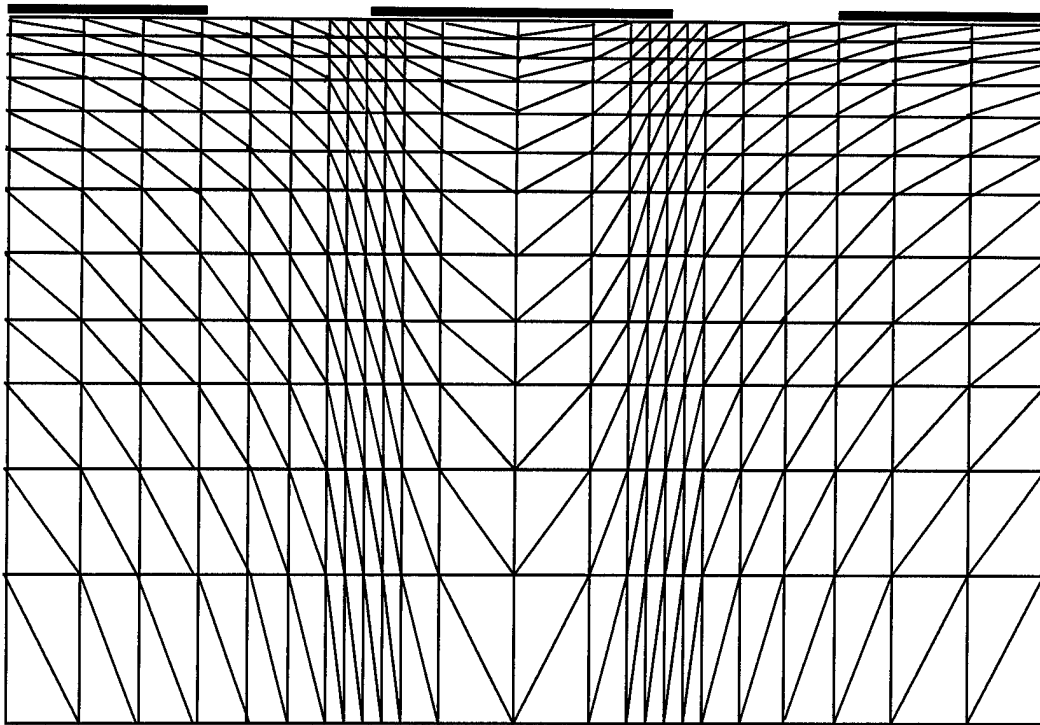


Fig. 5.1 Illustration of a typical mesh of a FET device for numerical solution of the hydrodynamic equations.

In this work, the spatial discretization is performed by using the Box Integration Method (BIM) [32]. The Box Integration Method is a generalization of the finite difference method. Within this method, each node of the mesh is surrounded by a subdomain (box). Each box is defined by the normal bisectors of the sides emanating from a given node, as shown in Fig. 5.2.

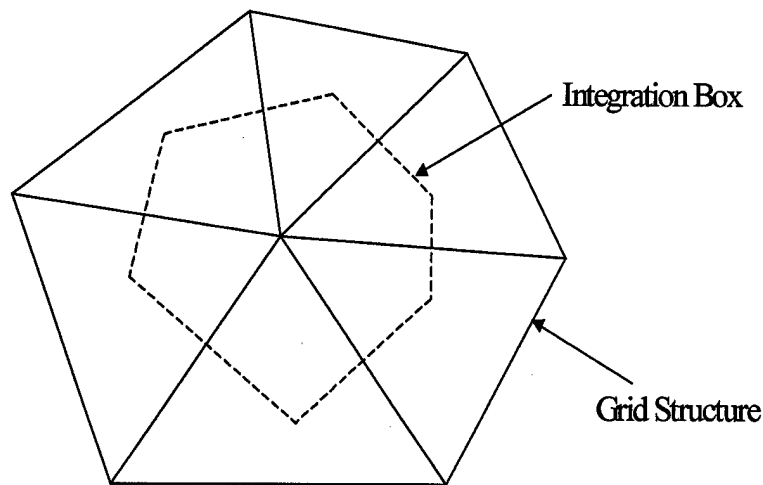


Fig. 5.2 Sample of Box Integration Method

We integrate the hydrodynamic balance equations over a subdomain. The divergence operator are integrated using Gauss' theorem. So that, we have the following equations:

$$\int_{\Gamma_i} \vec{D} \cdot \vec{i}_n d\Gamma_i = e \int_{\Omega_i} (p - n + N_D^+ - N_A^-) d\Omega_i, \quad (5.1)$$

$$\int_{\Gamma_i} \vec{J}_n \cdot \vec{i}_n d\Gamma_i = e \int_{\Omega_i} \frac{\partial n}{\partial t} d\Omega_i + e \int_{\Omega_i} U d\Omega_i, \quad (5.2)$$

$$\int_{\Gamma_i} \vec{J}_p \cdot \vec{i}_n d\Gamma_i = -e \int_{\Omega_i} \frac{\partial p}{\partial t} d\Omega_i - e \int_{\Omega_i} U d\Omega_i, \quad (5.3)$$

$$\int_{\Gamma_i} \vec{S}_n \cdot \vec{i}_n d\Gamma_i = - \int_{\Omega_i} \frac{\partial(nw_n)}{\partial t} d\Omega_i + \int_{\Omega_i} \left[E \cdot J_n - U w_n - n \left(\frac{w_n - w_0}{\tau_{nw}} \right) \right] d\Omega_i, \quad (5.4)$$

$$\int_{\Gamma_i} \vec{S}_p \cdot \vec{i}_n d\Gamma_i = - \int_{\Omega_i} \frac{\partial(pw_p)}{\partial t} d\Omega_i + \int_{\Omega_i} \left[E \cdot J_p - U w_p - p \left(\frac{w_p - w_0}{\tau_{pw}} \right) \right] d\Omega_i, \quad (5.5)$$

where Γ_i and Ω_i represent the boundary and the area of the i th box, respectively, and i_n is the external vector normal to Γ_i , as shown in Fig. 5.3.

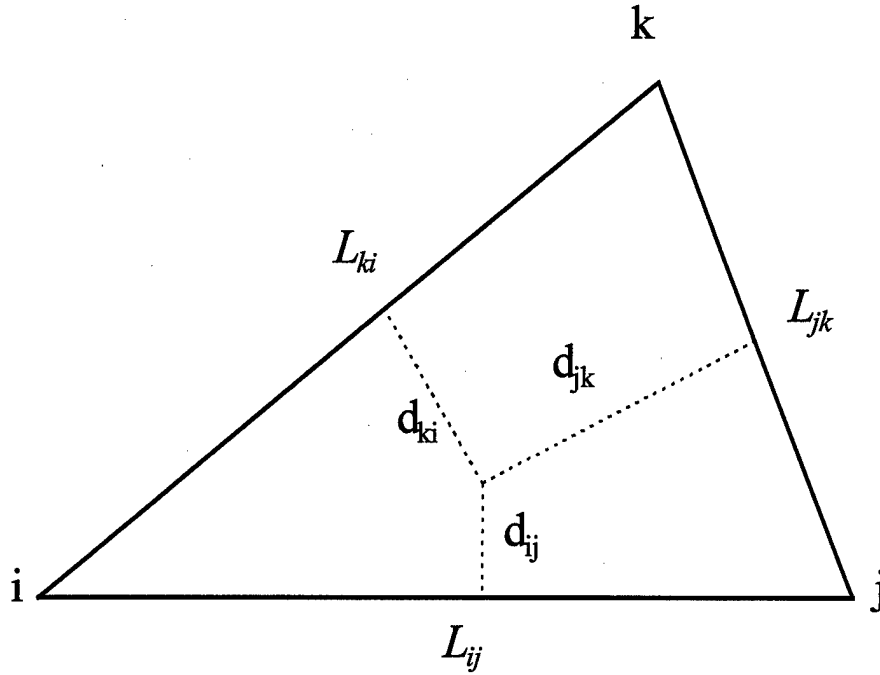


Fig. 5.3 The triangular elementary domain of the discretization grid.

The discrete form of the RHS of equations (5.1)-(5.5) is obtained by evaluating integrands at the node i and multiplying them by the box's area. For the left hand sides, we need to evaluate the flux of each vector through the boundary of the box. The discrete form of the LHS can be expressed as

$$\int_{\Gamma_i} \vec{F} \cdot \vec{i} d\Gamma_i = \sum_{i \neq j} d_{ij} F_{ij}, \quad (5.6)$$

where F_{ij} is the component of the flux flowing between node i enclosed by box Ω_i and a neighboring node j , and d_{ij} is the flux cross-section.

5.2 Poisson Equation

The electrical displacement vector projected over the element side (i, j) is:

$$D_{ij} = \frac{\epsilon}{L_{ij}} (\phi_i - \phi_j), \quad (5.7)$$

where L_{ij} is the length between node i and j . Under the assumption of the Boltzmann statistics, the relations of the electron and hole concentrations with the potentials can be written as

$$n = n_{ie} \exp \left\{ \frac{e(\phi - \psi_n)}{k_B T_e} \right\}, \quad (5.8)$$

$$p = n_{ie} \exp \left\{ \frac{e(\psi_p - \phi)}{k_B T_p} \right\}, \quad (5.9)$$

where n_{ie} is the effective intrinsic carrier concentration and ψ_n and ψ_p are the quasi-Fermi potential of electron and hole. The linearized Poisson equation is thus slightly changed from its standard form, and now reads

$$\nabla \cdot \delta D_{ij} + \left(\frac{e^2 n}{k_B T_e} + \frac{e^2 p}{k_B T_p} \right) \delta \phi = -\nabla \cdot D_{ij} + e(p - n + N_D^+ - N_A^-), \quad (5.10)$$

where δD_{ij} is defined by

$$\delta D_{ij} = \frac{\varepsilon}{L_{ij}} (\delta \phi_i - \delta \phi_j), \quad (5.11)$$

and $\delta \phi$ is a slight deviation of the electric potential. By using the Box Integration Method, we have the discretized Poisson equation for a slight deviation of the electrical potential

$$\sum_{j \neq i} d_{ij} \delta D_{ij} + \delta \phi \left(\frac{e^2 n}{k_B T_e} + \frac{e^2 p}{k_B T_p} \right) \Omega_i = -\sum_{j \neq i} d_{ij} D_{ij} + e(p - n + N_D^+ - N_A^-) \Omega_i. \quad (5.12)$$

5.3 Momentum Balance Equation

The discretization of momentum and energy balance equations is carried out by a generalization of the Scharfetter-Gummel discretization scheme [33,34]. The balance equations are projected onto the side L_{ij} and the projections are assumed to be constant over the side. And we notice that the first order differential equation of the form

$$\frac{dy}{dx} + P(x)y = Q(x), \quad (5.13)$$

has an integral solution of the form

$$y(x) = e^{-\int_0^x d\eta P(\eta)} \left[y(0) + \int_0^x d\eta Q(\eta) e^{\int_0^\eta d\xi P(\xi)} \right]. \quad (5.14)$$

Equation (5.13) can be rewritten as

$$\frac{y_j}{\int_{x_i}^{x_j} d\eta Q(\eta) e^{\int_{x_j}^\eta d\xi P(\xi)}} - \frac{y_i}{\int_{x_i}^{x_j} d\eta Q(\eta) e^{\int_{x_i}^\eta d\xi P(\xi)}} = 1. \quad (5.15)$$

The second term on the left-hand side of (4.32), which is the convective term, is generally small and is taken to be zero. Thus, the electron current density is projected onto the element side L_{ij} leading to a first order differential equation

$$\frac{J_{n_{ij}}}{\left(\frac{en k_B T_e v}{f} \right)} = \frac{dn}{dx_{ij}} + \left(\frac{1}{T_e} \frac{dT_e}{dx_{ij}} - \frac{e}{k_B T_e} \frac{d\phi}{dx_{ij}} \right) n, \quad (5.16)$$

where x_{ij} is the coordinate on the side L_{ij} . In order to implement the integration, we make an approximation that electron temperature, electric potential and total resistive force density are piecewise linear between two adjacent nodes. With the help of the Scharfetter-Gummel method, the current density along the mesh line between two adjacent nodes i and j can be expressed as [21,26]

$$J_{nij} = ek_B \left(\frac{\overline{nvT_e}}{f} \right)_{ij} \frac{T_{ej} - T_{ei}}{L_{ij} \ln(T_{ej} - T_{ei})} \left[B(\Delta_{ij}) \frac{n_j}{T_{ej}} - B(-\Delta_{ij}) \frac{n_i}{T_{ei}} \right], \quad (5.17)$$

where $B(\Delta)$ is the Bernoulli function

$$B(\Delta) = \frac{\Delta}{\exp(\Delta) - 1}, \quad (5.18)$$

and

$$\Delta_{ij} = \frac{\ln(T_{ej} - T_{ei})}{T_{ej} - T_{ei}} \left[\frac{e}{k_B} (\phi_j - \phi_i) - 2(T_{ej} - T_{ei}) \right]. \quad (5.19)$$

The symbol $\overline{\xi_{ij}}$ stands for the expectation value of an arbitrary variable ξ over L_{ij} . Further, we assume an exponential variation of the electron concentration along the side L_{ij}

$$n = n_i \exp(\alpha x_{ij}), \quad (5.20)$$

with

$$\alpha = \frac{1}{L_{ij}} \ln\left(\frac{n_j}{n_i}\right), \quad (5.21)$$

where n_i and n_j are the electron concentrations at node i and j . Thus, the expectation value of the electron concentration is given by

$$\bar{n}_{ij} = \frac{1}{L_{ij}} \int_{x_i}^{x_j} n dx = \frac{n_j - n_i}{\ln(n_j) - \ln(n_i)}. \quad (5.22)$$

The drift velocity between two nodes can be obtained by means of $J_{ij} = -e\bar{n}_{ij}v$. Therefore, the discretized momentum balance equation is

$$\sum_{j \neq i} d_{ij} J_{nij} = e \left(\frac{\partial n}{\partial t} + U \right)_i \Omega_i. \quad (5.23)$$

Similarly, the discretized form of the hole current density is expressed as

$$J_{pij} = -ek_B \left(\frac{\overline{pvT_p}}{f} \right)_{ij} \frac{T_{pj} - T_{pi}}{L_{ij} \ln(T_{pj} - T_{pi})} \left[B(\Delta_{ij}) \frac{p_j}{T_{pj}} - B(-\Delta_{ij}) \frac{p_i}{T_{pi}} \right], \quad (5.24)$$

where

$$\Delta_{ij} = -\frac{\ln(T_{pj} - T_{pi})}{T_{pj} - T_{pi}} \left[\frac{e}{k_B} (\phi_j - \phi_i) + 2(T_{pj} - T_{pi}) \right]. \quad (5.25)$$

5.4 Energy Balance Equation

We use a similar procedure for the energy balance equation. The electron energy flow density is rewritten as

$$\bar{S}_n = -\kappa_n \nabla T_e - \left(\frac{5}{2} k_B T_e \right) \frac{\bar{J}_n}{e}. \quad (5.26)$$

Then (4.31) can be expressed as

$$\frac{\partial(nw_n)}{\partial t} + \nabla \cdot \bar{S}_n = \nabla \cdot \left(\frac{m|\bar{J}_n|^2}{2e^2 n^2} - e\phi \right) \frac{\bar{J}_n}{e} - U w_n - W. \quad (5.27)$$

The electron energy flux density is projected onto the element side L_{ij} leading to a first order differential equation

$$S_{n_{ij}} = -\kappa_n \frac{dT_e}{dx_{ij}} - \frac{J_{n_{ij}}}{e} \frac{5}{2} k_B T_e. \quad (5.28)$$

Employing the Scharfetter-Gummel method, the discretization of the energy flow density can be written as [16,27,35]:

$$S_{n_{ij}} = -\frac{\bar{\kappa}_{n_{ij}}}{L_{ij}} \left[B(\omega_{ij}) T_{e_j} - B(-\omega_{ij}) T_{e_i} \right], \quad (5.29)$$

where

$$\bar{\kappa}_{n_{ij}} = \left(\frac{5}{2} + c \right) k_B^2 \left(\frac{nvT_e}{f} \right)_{ij} \bar{n}_{ij}, \quad (5.30)$$

$$\omega_{ij} = -\frac{5}{2} k_B \frac{J_{n_{ij}}}{e} \frac{L_{ij}}{\bar{\kappa}_{n_{ij}}}. \quad (5.31)$$

Finally, the discretized energy balance equation is

$$\left[\frac{\partial(nw_n)}{\partial t} \right]_i \Omega_i + \sum_{j \neq i} d_{ij} S_{n_{ij}} = \sum_{j \neq i} d_{ij} \frac{J_{n_{ij}}}{e} \left(\frac{m_n J_n^2}{2e^2 n^2} \right)_{ij} + \left[\langle \bar{E} \cdot \bar{J}_n \rangle - U w_n - W \right]_i \Omega_i. \quad (5.32)$$

Similarly, the discretized form of the hole energy flux density is expressed as

$$S_{p_{ij}} = -\frac{\bar{\kappa}_{p_{ij}}}{L_{ij}} \left[B(\omega_{ij}) T_{p_j} - B(-\omega_{ij}) T_{p_i} \right], \quad (5.33)$$

where

$$\bar{\kappa}_{p_{ij}} = \left(\frac{5}{2} + c \right) k_B^2 \left(\frac{pvT_p}{f} \right)_{ij} \bar{p}_{ij}, \quad (5.34)$$

$$\omega_{ij} = \frac{5}{2} k_B \frac{J_{p_{ij}}}{e} \frac{L_{ij}}{\bar{\kappa}_{p_{ij}}}. \quad (5.35)$$

5.5 The Numerical Method for the Transient Problem

The time discretization for the carrier continuity and the energy balance equation we used here is the Crank-Nicolson implicit scheme [36], which is second-order accurate in time and is usually stable for large time steps. Applying this scheme to the carrier continuity and the energy balance equation, we have

$$\frac{n^{t+1} - n^t}{\Delta t} = \frac{1}{2} \left(\frac{1}{e} \nabla \cdot J^t \right) + \frac{1}{2} \left(\frac{1}{e} \nabla \cdot J^{t+1} \right), \quad (5.36)$$

$$\begin{aligned} \frac{(nw)^{t+1} - (nw)^t}{\Delta t} = & \frac{1}{2} \left\{ \nabla \cdot \left(\frac{m |\bar{J}^t|^2}{2e^2 n^{t2}} - e \phi^t \right) \frac{\bar{J}^t}{e} - \nabla \cdot \bar{S}^t - W^t \right\} \\ & + \frac{1}{2} \left\{ \nabla \cdot \left(\frac{m |\bar{J}^{t+1}|^2}{2e^2 n^{t+12}} - e \phi^{t+1} \right) \frac{\bar{J}^{t+1}}{e} - \nabla \cdot \bar{S}^{t+1} - W^{t+1} \right\}. \end{aligned} \quad (5.37)$$

Our simulation process starts with the potential solution

$$\nabla^2 \phi^{t+1} = -\frac{e}{\epsilon} (N_D - n^{t+1}). \quad (5.38)$$

While solving for the potential ϕ^{t+1} at time level (t+1), the carrier concentration n^{t+1} at (t+1) is not available. So that, we need to know the value of the carrier density. If we employed the fully explicit scheme into (5.2), then we have the differential form of the carrier continuity equation

$$\frac{n^{t+1} - n^t}{\Delta t} = \left(\frac{1}{e} \nabla \cdot \bar{J}_n - U \right)^t. \quad (5.39)$$

Thus, the approximate solution of the carrier concentration at time level (t+1) is

$$n_a^{t+1} = n^t + \Delta t \cdot \frac{1}{e} \nabla \cdot J_n^t - \Delta t \cdot U. \quad (5.40)$$

We put this approximate solution into the Poisson equation to obtain a modified Poisson equation [37]

$$\nabla^2 \phi^{t+1} = -\frac{e}{\epsilon} (N_D - n^t - \Delta t \cdot \frac{1}{e} \nabla \cdot J_n^t + \Delta t \cdot U), \quad (5.41)$$

where n^t and J_n^t are the carrier density and current density at time level (t), respectively.

To avoid the nonconservation of charge during the transient state, the potential distribution should be corrected at each time step by solving the Poisson equation [38]. Thus, after obtaining a solution of one of the time-dependent hydrodynamic balance equations, a procedure to correct the Poisson equation is necessary to ascertain a self-consistent solution.

We will use the solution of the modified Poisson equation to update the quasi-Fermi potential

$$\psi_n^{t+1} = \phi^{t+1} - \frac{k_B T_e^t}{e} \ln \left(\frac{n_a^{t+1}}{n_{ie}} \right). \quad (5.42)$$

Following that, we put this quasi-Fermi potential into the Poisson equation to obtain the accurate potential at time level (t+1). We use an iterative process to solve Poisson equation with the quasi-Fermi potential kept constant [31]. After solving the Poisson equation, we have an accurate potential at time level (t+1). We use this new quasi-Fermi potential and the new potential to calculate the total resistive force density at time level (t+1), f^{t+1} , and use this f^{t+1} in Eq. (5.17) to get the current density at time level (t+1). In this way, we can solve the carrier continuity equation. Because the carrier density has

already changed, this caused the electric potential to change, too. For self-consistency, we need to solve the Poisson equation again.

The solution n^{t+1} is used to update the quasi-Fermi potential ψ_n , which is given by [25]

$$\psi_n^{t+1} \leftarrow \psi_n^{t+1} - \frac{k_B T_e^t}{e} \ln\left(\frac{n^{t+1}}{n_a^{t+1}}\right). \quad (5.43)$$

Then we put this quasi-Fermi potential into the Poisson equation to obtain the new potential and the new electron density at time level (t+1). We use all these new solutions to calculate the total resistive force density f^{t+1} and the energy-loss rate W^{t+1} .

With all these data at time level (t+1), we can solve the energy balance equation (5.37). After solving the energy balance equation, the electron temperature at time level (t+1) is obtained, which is used to update the quasi-Fermi potential first. The updated quasi-Fermi potential is given by

$$\psi_n^{t+1} = \phi^{t+1} - \frac{k_B T_e^{t+1}}{e} \ln\left(\frac{n^{t+1}}{n_{ie}}\right). \quad (5.44)$$

The new electron temperature will affect the electron concentration distribution, and in turn, the electric potential. Thus, we need to solve the Poisson equation again to get the accurate electric potential and electron density. Here we have all the solutions at time level (t+1), which can be used as initial solutions to solve all the equations again. The iterative process will come to an end when the total time is equal to a predetermined length of time, e.g., 10 ps. The flow chart of the transient simulation procedure is shown in the Fig. 5.4.

For the automatic time step selection, there is a little difference between our method and [39]. We utilized the relative difference δ^* between the exact solution and the approximate solution of the carrier density at time level (t+1) to select a new time step. If we take a time step and produce δ^* , the new time step will be estimated as

$$\Delta t^* = g \Delta t, \quad g = s \left| \frac{\delta_0}{\delta^*} \right|^{0.5}, \quad S = \begin{cases} 0.9995 & \delta^* \geq \delta_0 \\ 1 & \delta^* < \delta_0 \end{cases}, \quad (5.45)$$

and

$$\delta^* = \frac{|n^{t+1} - n_a^{t+1}|}{n^{t+1}}, \quad (5.46)$$

where s is a safety factor and δ_0 is the given tolerance which is chosen to be 0.008 in the following example. If δ^* is larger than δ_0 , the new time step will decrease. On the other hand, when δ^* is smaller than δ_0 , the time step size will increase for the next iteration. Special care is taken not to let the time step grow too fast. Here, we restrict the value of g by a factor 1.2.

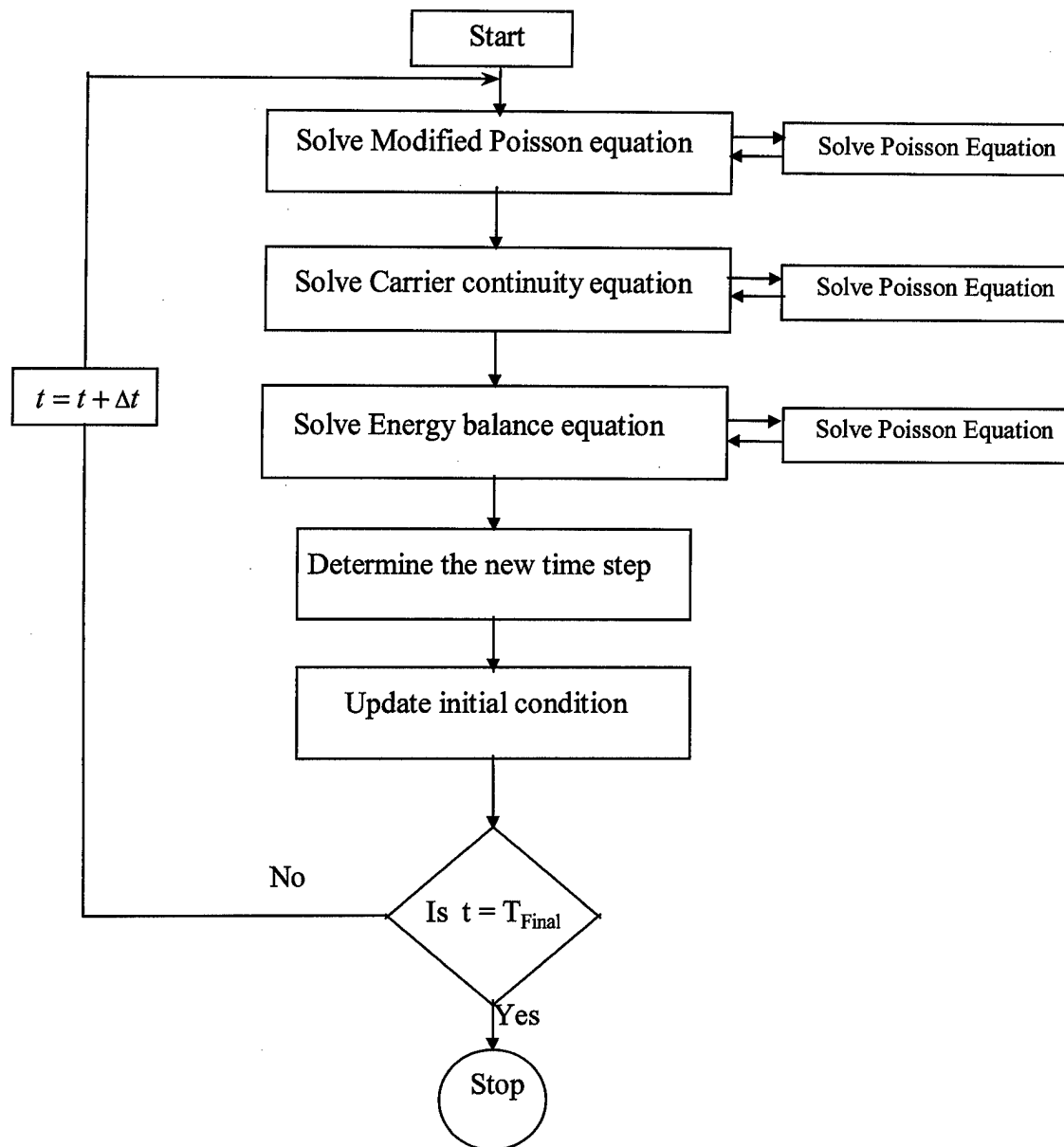


Fig. 5.4 Flow chart of transient solution procedure.

6. Device Simulation Results

We have applied our hydrodynamic balance equations to the simulation of one-dimensional and two-dimensional submicron Si devices. Scattering mechanisms considered are ionized impurity scattering, acoustic phonon scattering via deformation potential coupling, and nonpolar optical phonon scattering. In this work, we included static screening only.

6.1 One Dimensional Si $n^+ - n - n^+$ Diode

Here, a one-dimensional submicron $n^+ - n - n^+$ diode has been simulated. It has some resemblance to the n-channel of a silicon MOSFET. Although this device is rather simple, it is very useful for investigating basic transport phenomena. It is also simple enough to do a Monte Carlo simulation, so that the latter may be compared with our results. Further, there are so many different device modeling attempts on such a device, so that we can readily compare our results with those obtained with different approaches. This device is a $0.6\text{ }\mu\text{m}$ silicon structure with a symmetric doping profile. Its inner region is $0.4\text{ }\mu\text{m}$ long with a doping level of $N_D = 2 \times 10^{15}\text{ cm}^{-3}$, while the emitter and collector are each $0.1\text{ }\mu\text{m}$ long with a doping $N_D = 5 \times 10^{17}\text{ cm}^{-3}$. There is smooth grading of the doping level at the junctions between the electrodes and the inner region. The mesh point spacing can be uniform or nonuniform. Here we used 60-node grids that are uniformly distributed along the device length. The grid spacings are $\Delta x = 0.01\text{ }\mu\text{m}$. We chose the lattice temperature T_0 to be 300K.

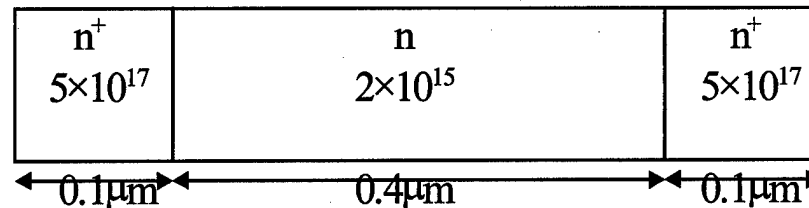


Fig. 6.1 Ballistic diode

6.1.1 Steady State Simulation

We have applied the multi-valley Lei-Ting balance equation to a six-valley system (silicon). The intravalley acoustic-phonon scattering and six phonon models of intervalley scattering are considered. Here the energy band structure is taken to be parabolic.

In our simulation of the device, we have the left terminal of the diode grounded ($V_L=0$), and a positive bias is applied to the right terminal ($V_R=V$), so that the electrons are injected from the left end and move toward the right end. We assume that the contacts are ideal ohmic contacts. From this assumption, it preserves charge neutrality and thermal equilibrium at the contacts. We used the following boundary conditions in this example:

$$T_e(L) = T_e(R) = T_0, \quad (6.1)$$

$$n(L) = N_D(L), \quad n(R) = N_D(R), \quad (6.2)$$

$$\phi(L) = \frac{k_B T_e}{e} \ln \left(\frac{n(L)}{n_{ie}} \right), \quad \phi(R) = \frac{k_B T_e}{e} \ln \left(\frac{n(R)}{n_{ie}} \right) + V, \quad (6.3)$$

where V is the applied bias. The electron velocity and normalized temperature are shown in Fig. 6.2 and 6.3. From our simulation results, we see that the drift velocity exhibit some overshoot at the high field region before it reaches the collector. The maximum drift velocity approaches the saturation velocity as the applied bias increases. The electron temperature also behaves as expected. All of our results are in general agreement with other available results, including details of velocity overshoot, obtained with Monte Carlo simulations [40,41]. We also note that the spurious overshoot peak, which usually exists in other hydrodynamic models when electric field drastically decreases, is absent in our result.

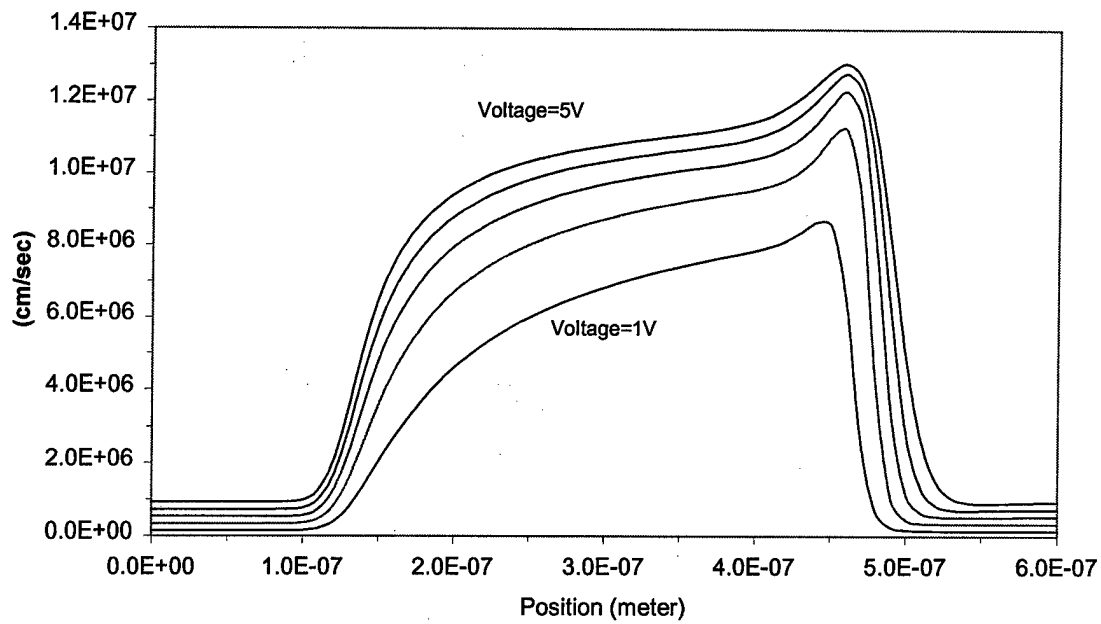


Fig. 6.2 Electron drift velocity as a function of position in the ballistic diode, under the bias voltage of 1V, 2V, 3V, 4V and 5V.

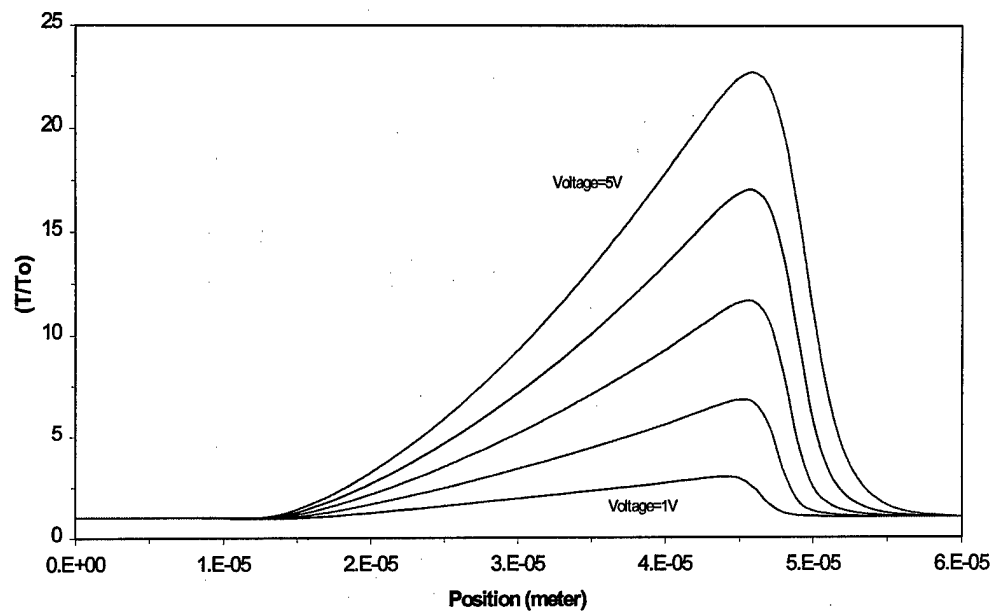


Fig. 6.3 Electron temperature as a function of position in the ballistic diode, under the bias voltage of 1V, 2V, 3V, 4V and 5V.

6.1.2 Transient Simulation

Here, we used the single parabolic hydrodynamic balance equation to perform the transient simulation.

The boundary conditions for temperature and electron concentration on the emitter and collector are the same as the steady state simulation. We applied the following equations for the electrostatic potential:

$$\phi(L) = \frac{k_B T_e}{e} \ln \left(\frac{n(L)}{n_{ie}} \right), \quad \phi(R) = \frac{k_B T_e}{e} \ln \left(\frac{n(R)}{n_{ie}} \right) + V(t), \quad (6.4)$$

where $V(t)$ is the applied bias. The initial conditions were obtained from the steady state solution with applied voltage $V=0$. Then at time $t=0$, we applied a step voltage to the anode.

Although the Crank-Nicolson scheme is an implicit time integration method, it still has stability problems related to the time step size[42]. In our simulation, the first time step is 1.0×10^{-15} s and the maximum time step is 5.0×10^{-14} s. Although we restricted the maximum time step to ensure stability, it is still an efficient method for transient simulation. For example, it only needed 221 time steps in the case of the 4V bias. From our simulation results, we see that the drift velocity exhibit some transient overshoot at the high field region before it reaches its steady state. The electron temperature also behaves as expected. All of our results are in general agreement with other available results, including details of velocity overshoot, obtained with other hydrodynamic simulations [43,44] and Monte Carlo simulations [45,46]. Velocity overshoot can improve the performance of small device because the average carrier velocity can exceed the steady state limit.

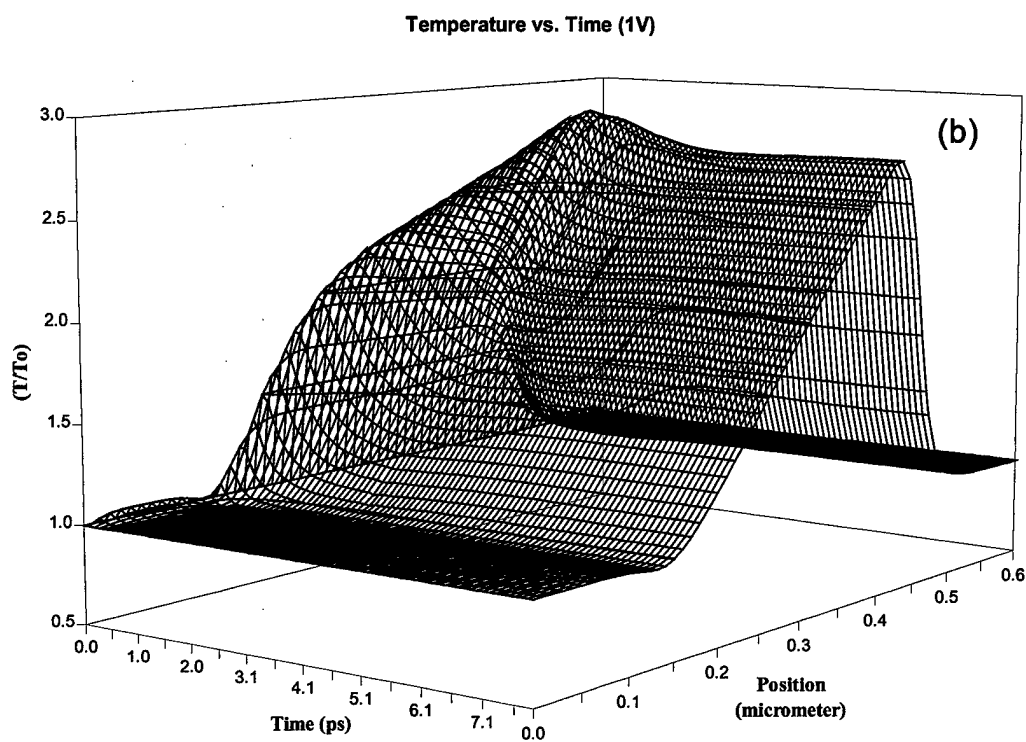
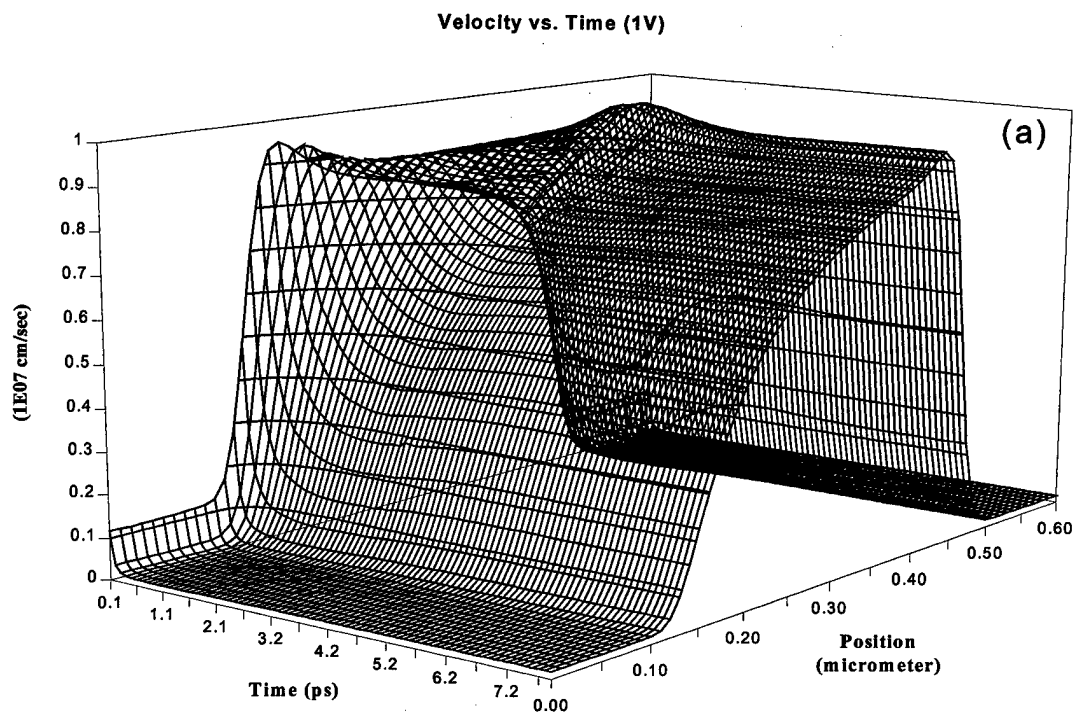


Fig. 6.4 (a) Electron drift velocity, (b) Electron temperature as functions of time and position along the device for a bias voltage of 1V.

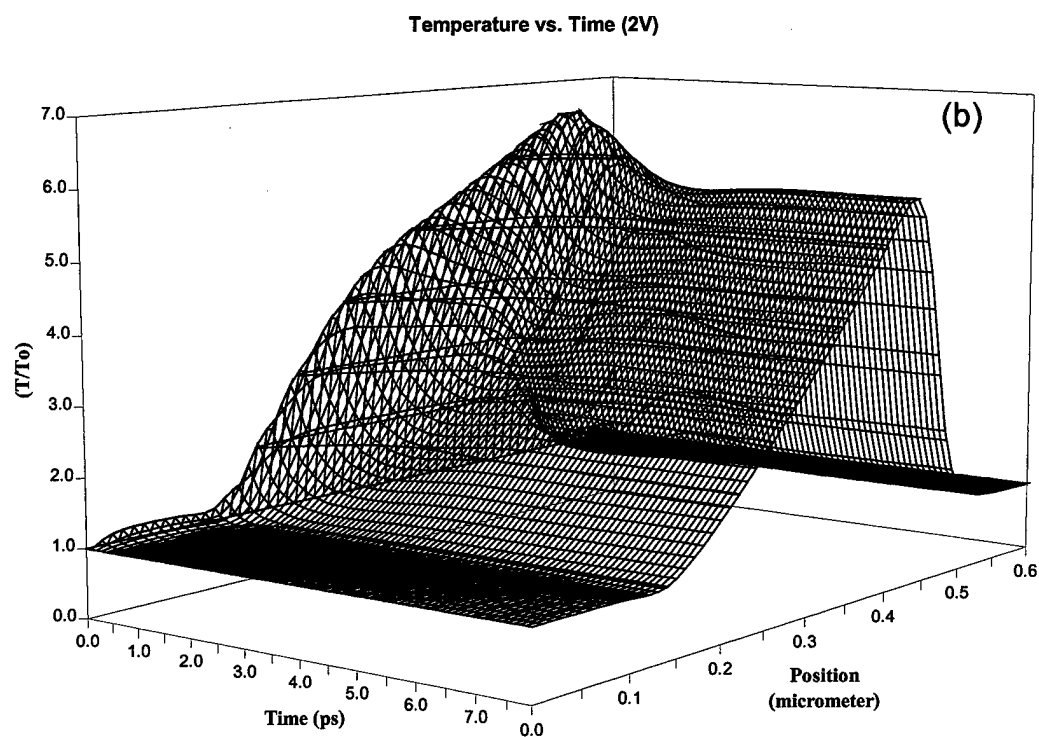
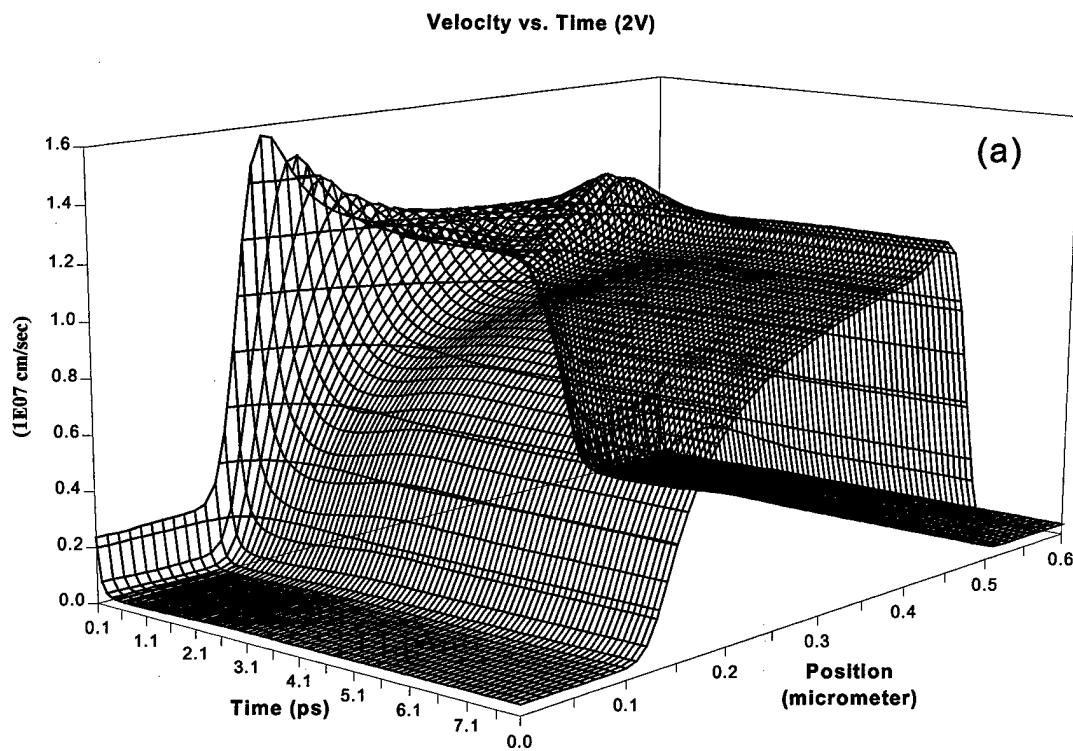


Fig. 6.5 (a) Electron drift velocity, (b) Electron temperature as functions of time and position along the device for a bias voltage of 2V.

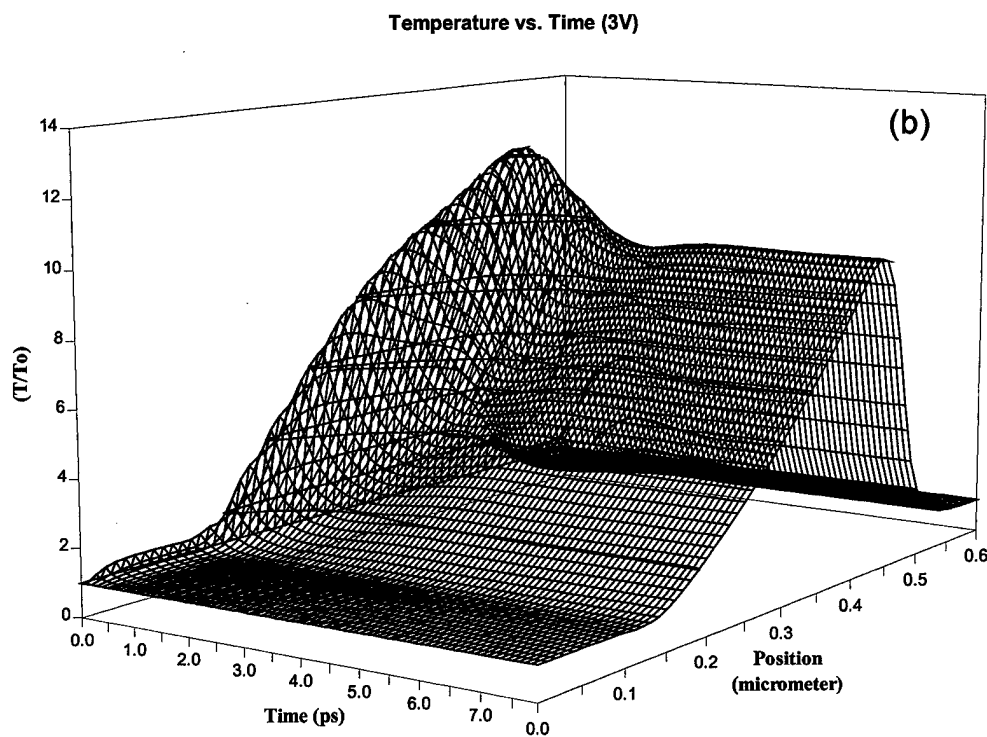
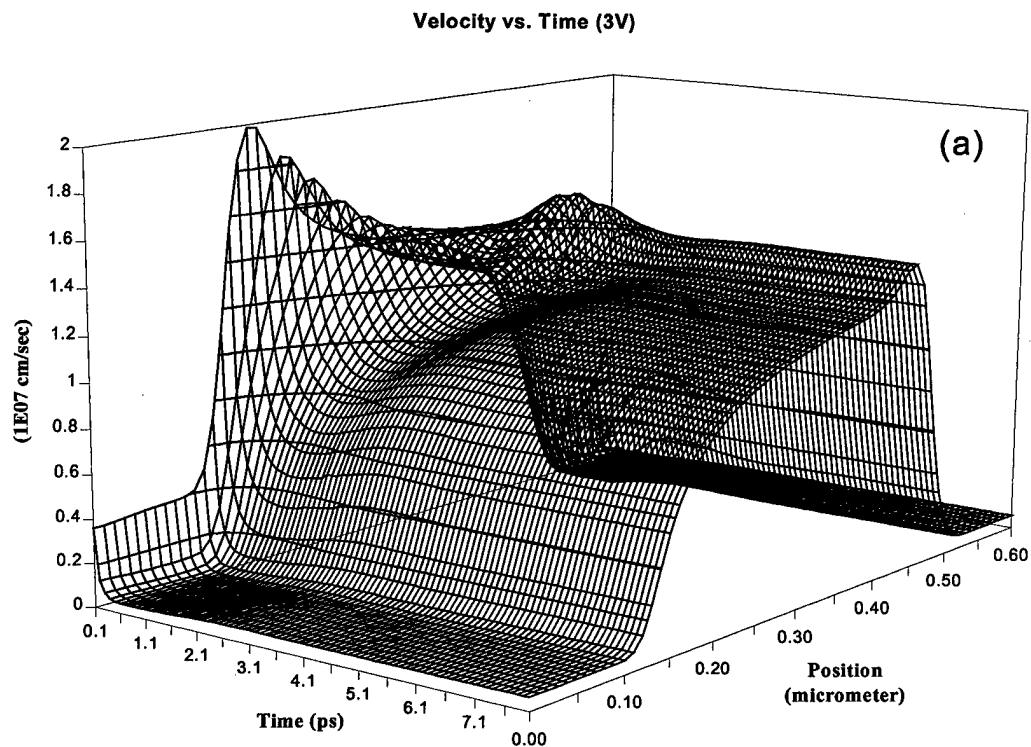


Fig. 6.6 (a) Electron drift velocity, (b) Electron temperature as functions of time and position along the device for a bias voltage of 3V.

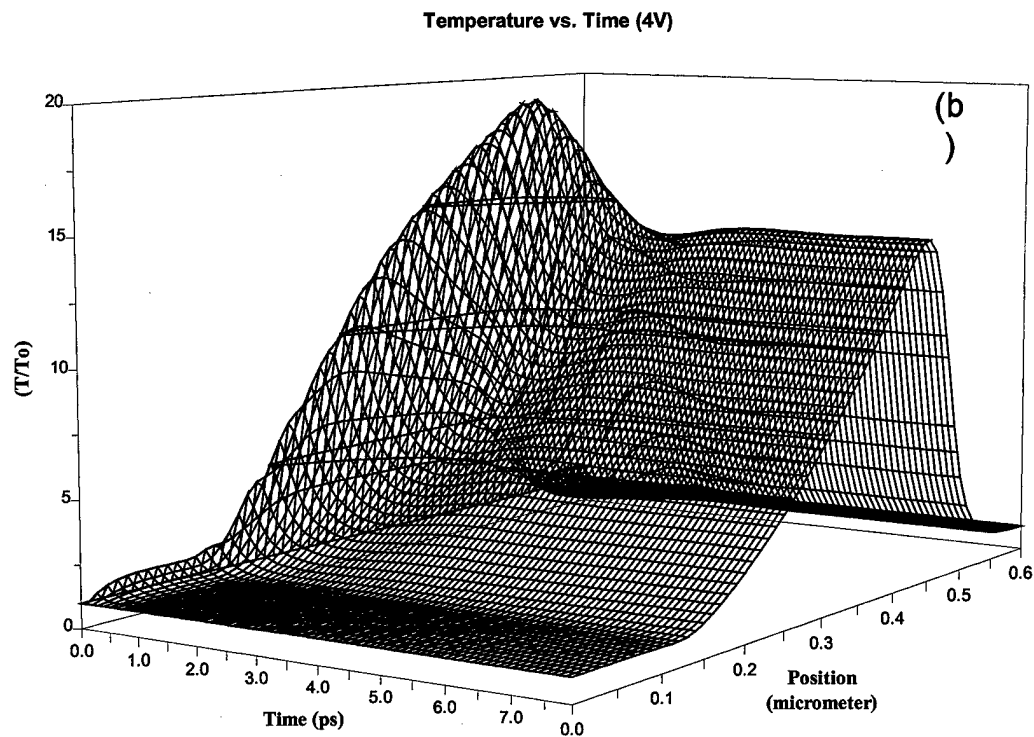
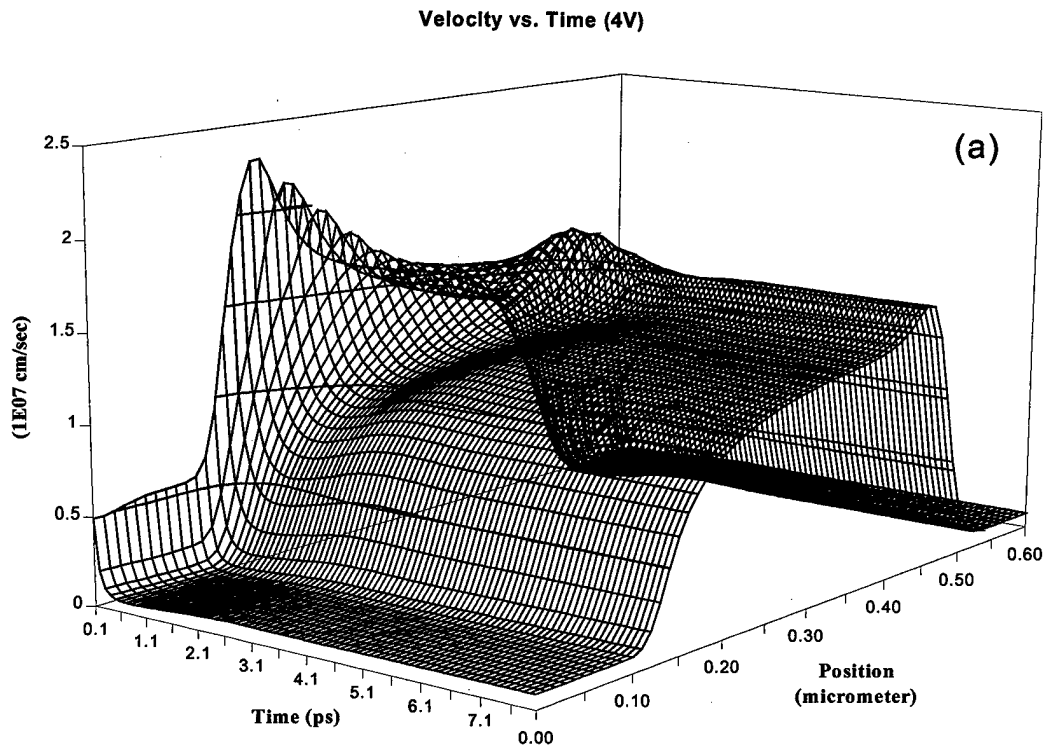


Fig. 6.7 (a) Electron drift velocity, (b) Electron temperature as functions of time and position along the device for a bias voltage of 4V.

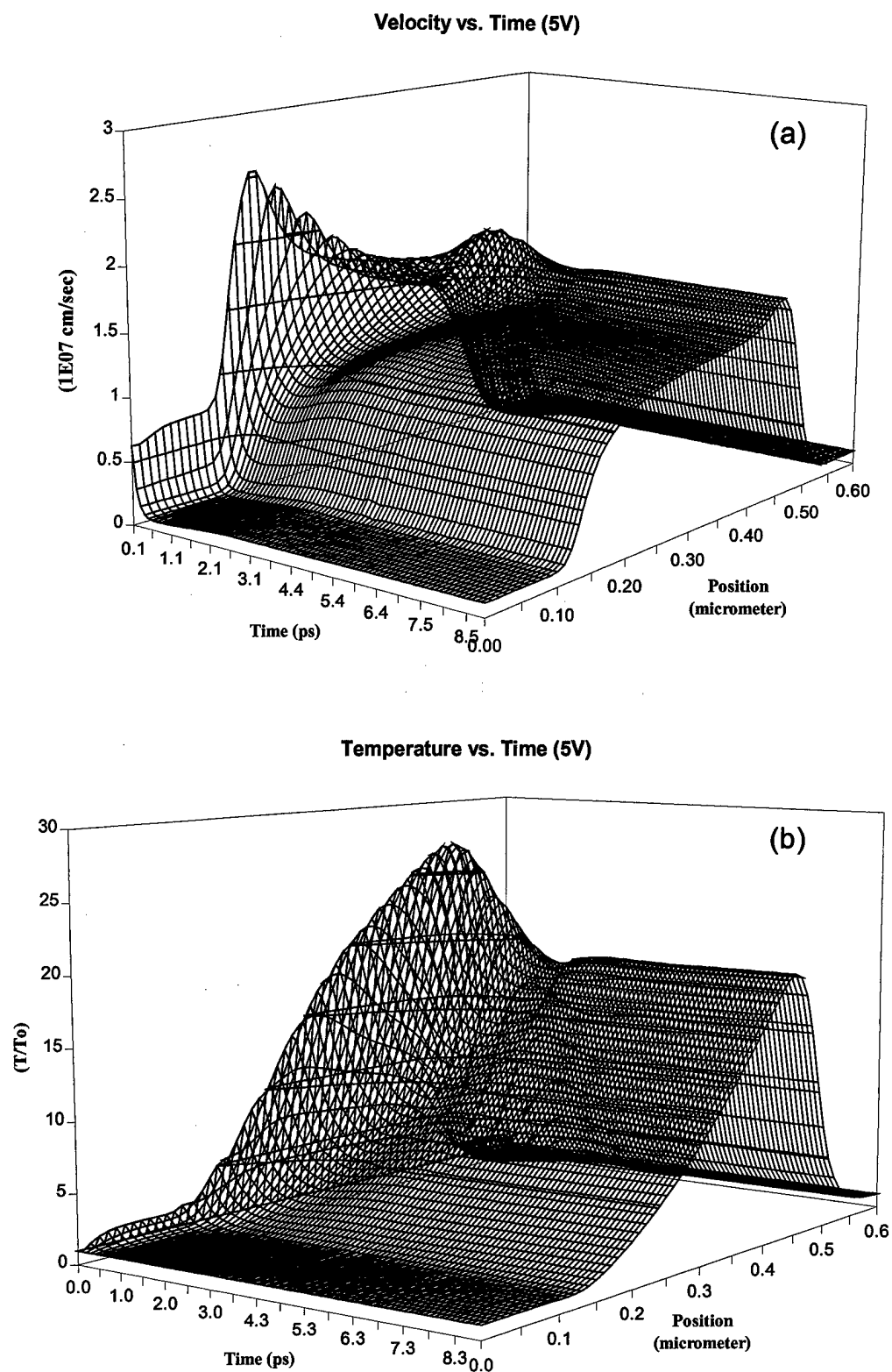


Fig. 6.8 (a) Electron drift velocity, (b) Electron temperature as functions of time and position along the device for a bias voltage of 5V.

6.2 Two Dimensional MESFET

We have applied the Lei-Ting hydrodynamic balance equations to the simulation of a two-dimensional MESFET of the size $0.6\mu\text{m} \times 0.2\mu\text{m}$. This device geometry and doping profile are depicted in Fig. 6.9. The substrate of the device is doped n-type with doping value of $1 \times 10^{17} \text{cm}^{-3}$. The two n^+ regions are of size $0.1\mu\text{m} \times 0.05\mu\text{m}$. The doping of these regions is $3 \times 10^{17} \text{cm}^{-3}$. This device is a special form of a junction field-effect transistor. The lattice temperature T_0 is taken as 300K.

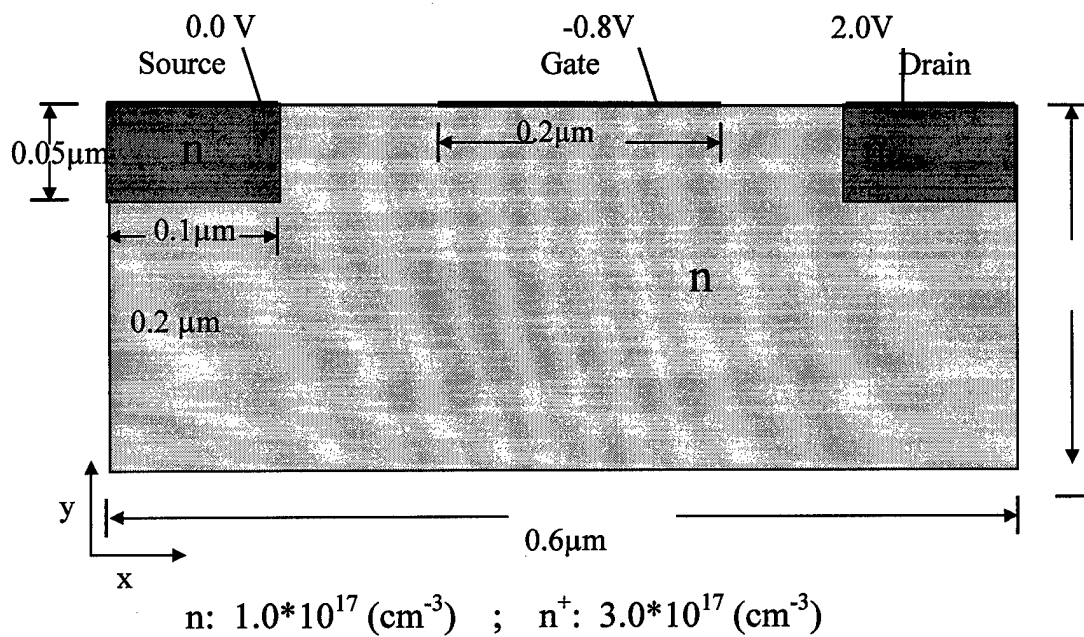


Fig. 6.9 A two-dimensional Silicon MESFET device.

6.2.1 Steady State Simulation

We apply a voltage bias 2V at the drain and a negative voltage bias -0.8V at the gate. For the boundary conditions, we assume the Schottky contact on the gate and the ideal ohmic contact on the source and drain. This example is the same as the device presented in (Aluru *et al.* 1994). For simplicity, a uniform rectangular grid is used here.

The equipotential contour plot is shown in the Fig. 6.10. The electron concentration is plotted in the Fig. 6.11. The profile of the normalized electron temperature is shown in the Fig. 6.12(a). We can see that the peak temperature is near the drain. The longitudinal electron velocity profile is shown in the Fig. 6.12(b). The spurious velocity overshoot spike which appears in the solutions with the hydrodynamic model (Aluru *et al.* 1994) is virtually absent in our results.

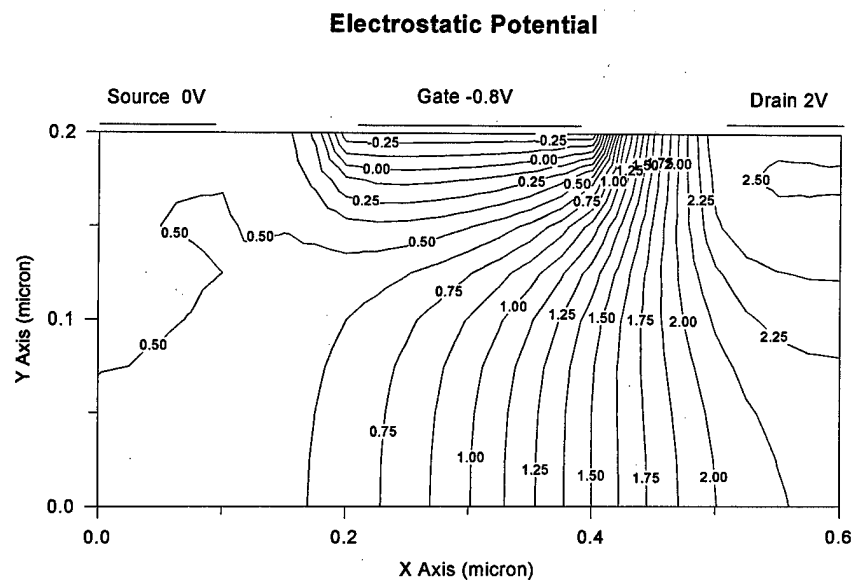


Fig. 6.10 Equipotential contour as a function of position.

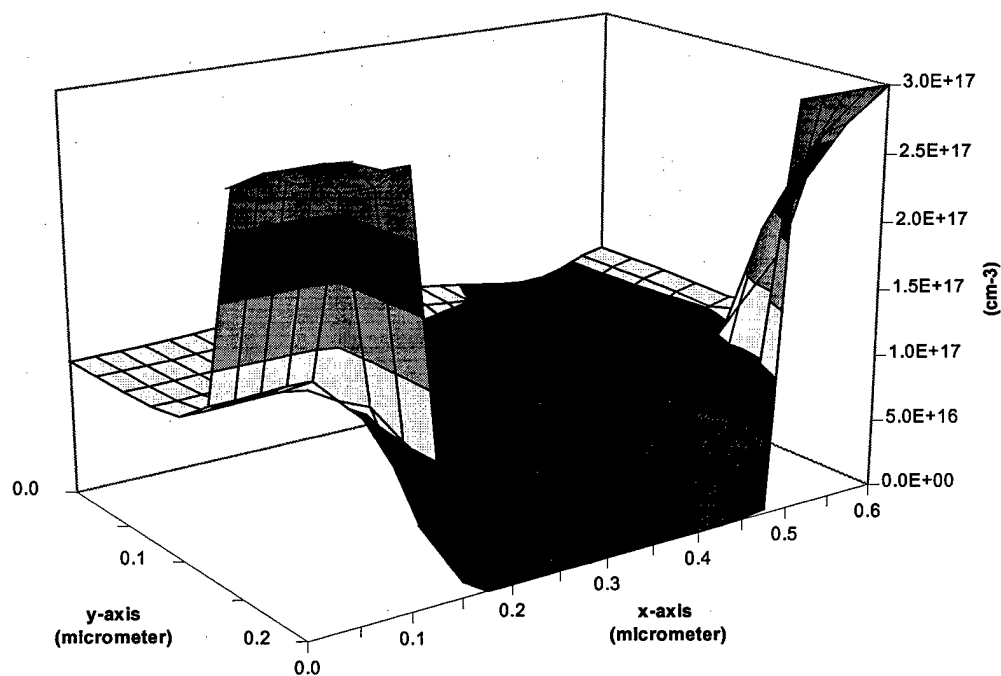


Fig. 6.11 Electron concentration as a function of position.

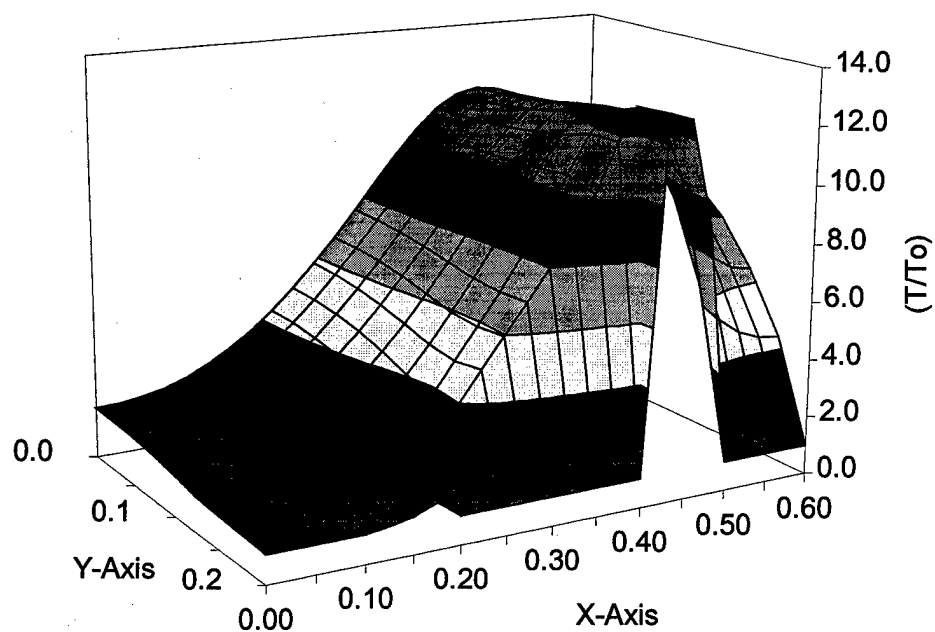


Fig. 6.12(a) Electron temperature as a function of position.

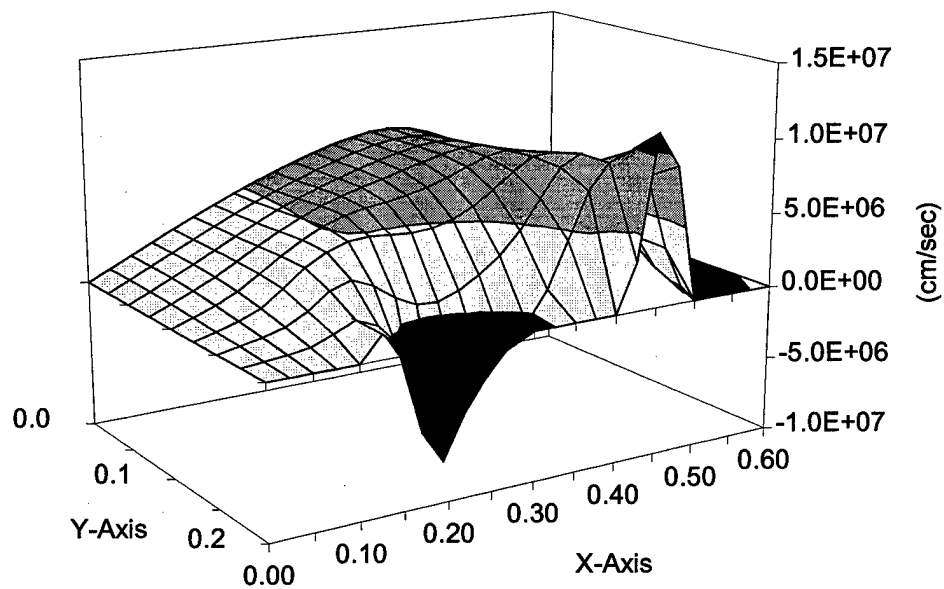


Fig. 6.12(b) Electron drift velocity as a function of position.

6.2.2 Transient State Simulation

We have also performed transient simulation of a two-dimensional MESFET [28]. The device is the same as before. The initial conditions were obtained from the steady state solution with applying a voltage bias 2V at the drain and a zero voltage bias at the gate. For the boundary conditions, we assume the Schottky contact on the gate and the ideal ohmic contact on the source and drain. Then at time $t = 0$, we applied a step negative voltage bias -0.8V at the gate.

In our simulation, the first time step is 1.0×10^{-16} s and the maximum time step is 1.0×10^{-14} s. Although we restricted the maximum time step to ensure stability, it is still an efficient method for transient simulation. From our simulation results, we see that the drift velocity exhibits some transient overshoot at the high field region before it reaches its steady state. The electron temperature also behaves as expected. All of our results are in general agreement with other available results, including details of velocity overshoot, obtained with other hydrodynamic simulations and Monte Carlo simulations. The simulation results are presented in the figures in the form of spatial distributions at various times during the entire transient process. These include the electron velocity, the electron temperature and the electric field. Also presented are equipotential contours as well as the terminal currents as functions of time.

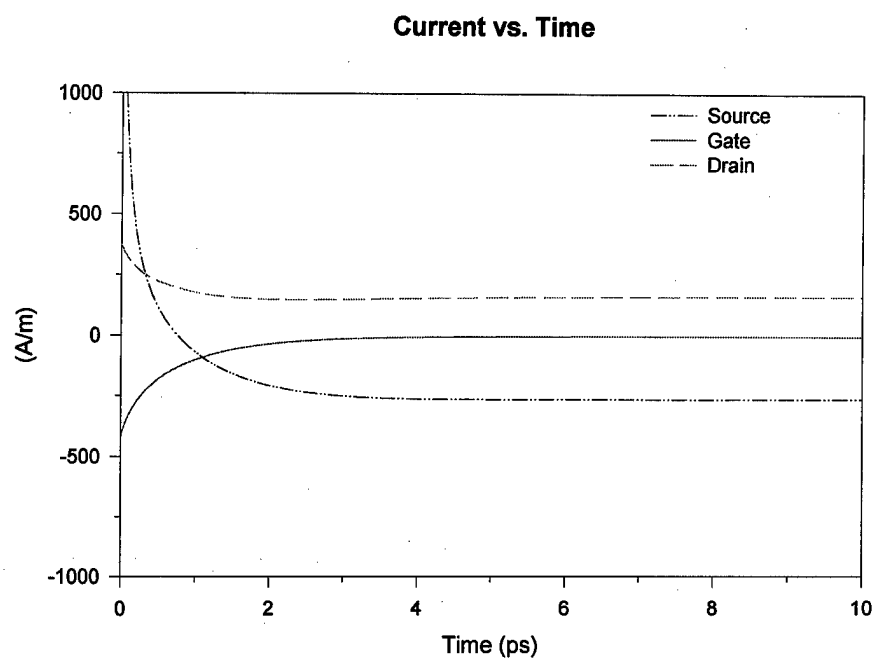


Fig. 6.13 Terminal currents as fuctions of time.

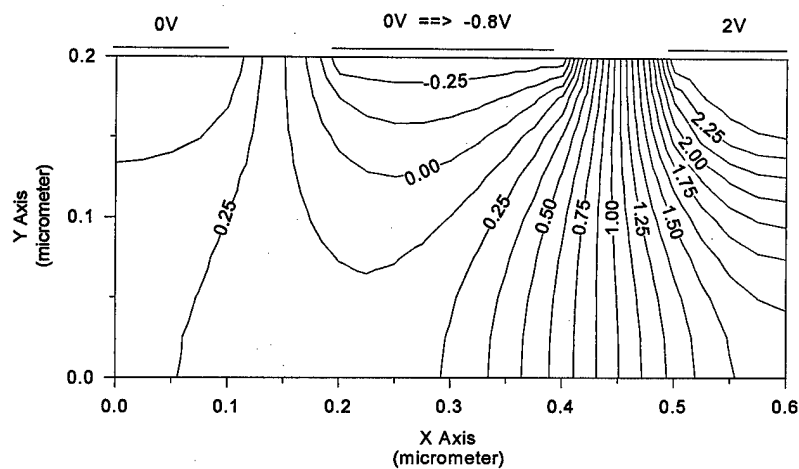


Fig. 6.14(a) Electrostatic potential at 0.05ps

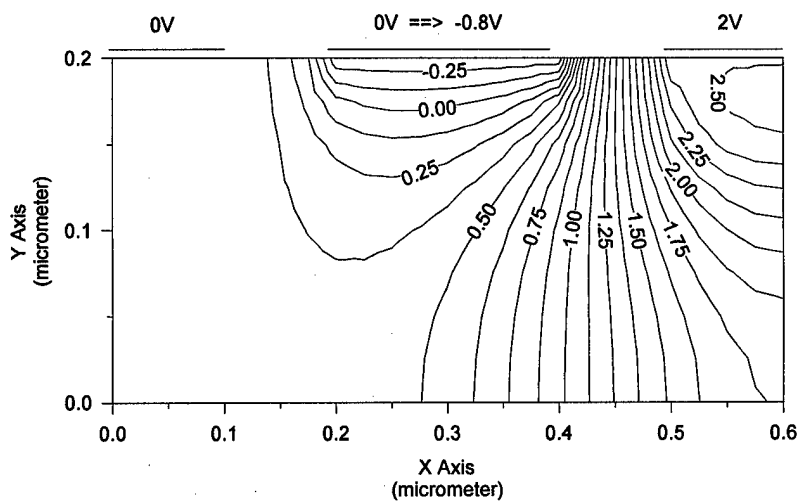


Fig. 7.14(b) Electrostatic potential at 0.5ps

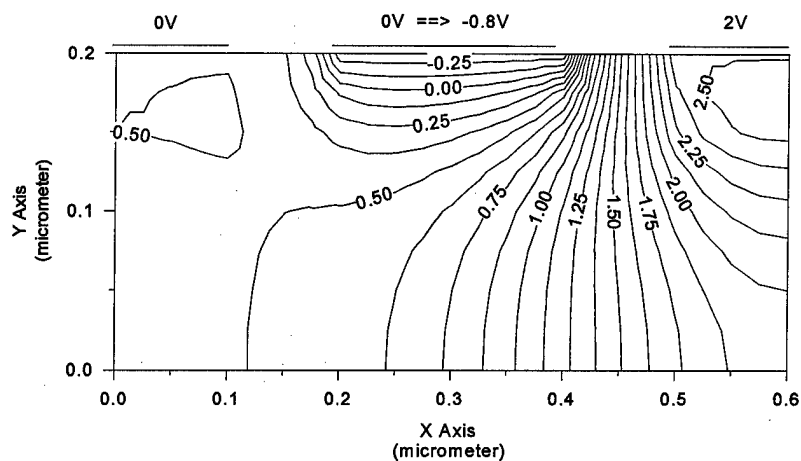


Fig. 7.14(c) Electrostatic potential at 1ps

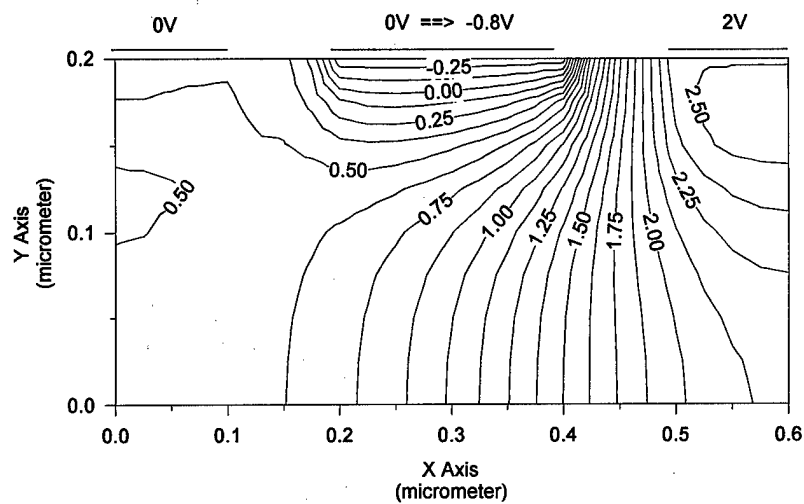


Fig. 7.14(d) Electrostatic potential at 2ps

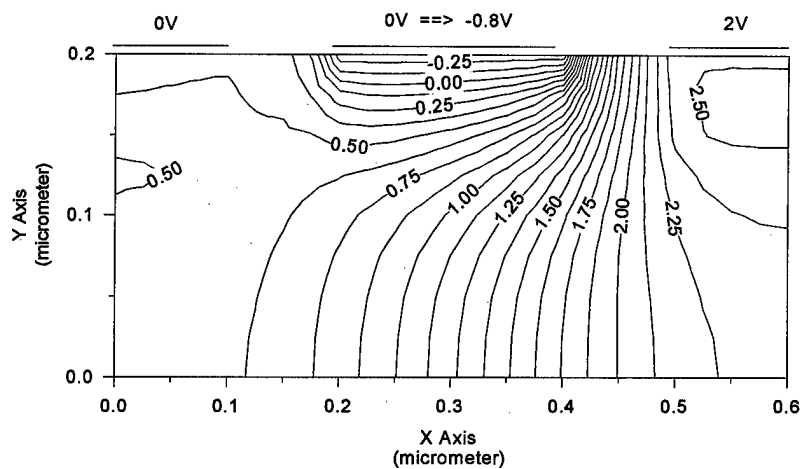


Fig. 7.14(e) Electrostatic potential at 5.5ps

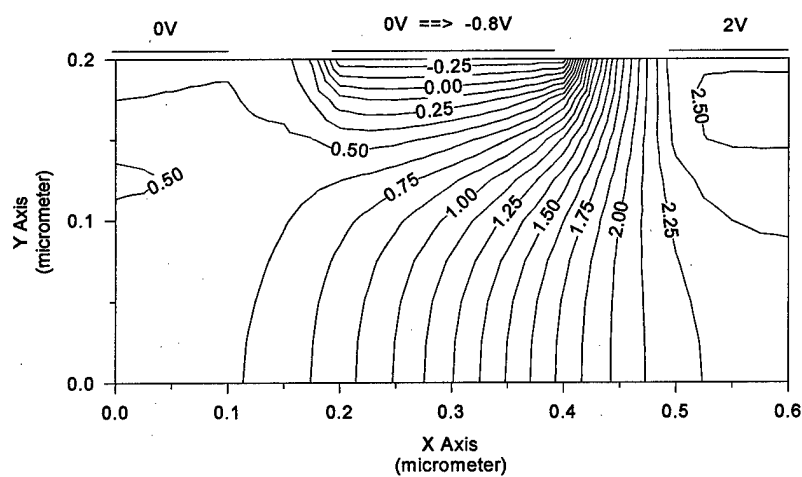


Fig. 7.14(f) Electrostatic potential at 10ps

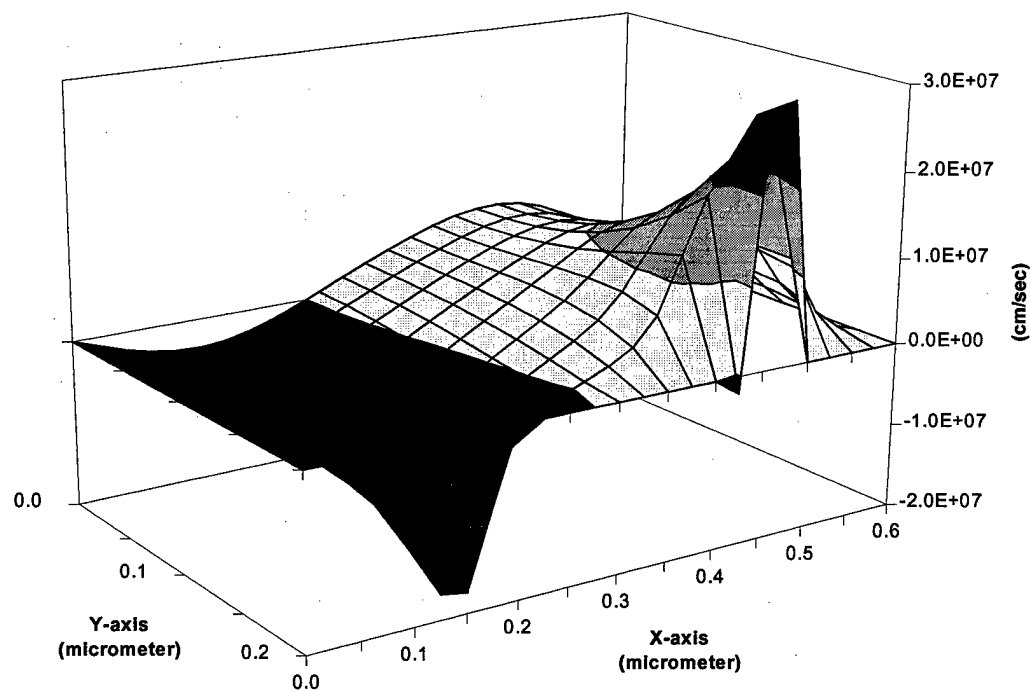


Fig. 6.15(a) Longitudinal velocity at 0.05ps.

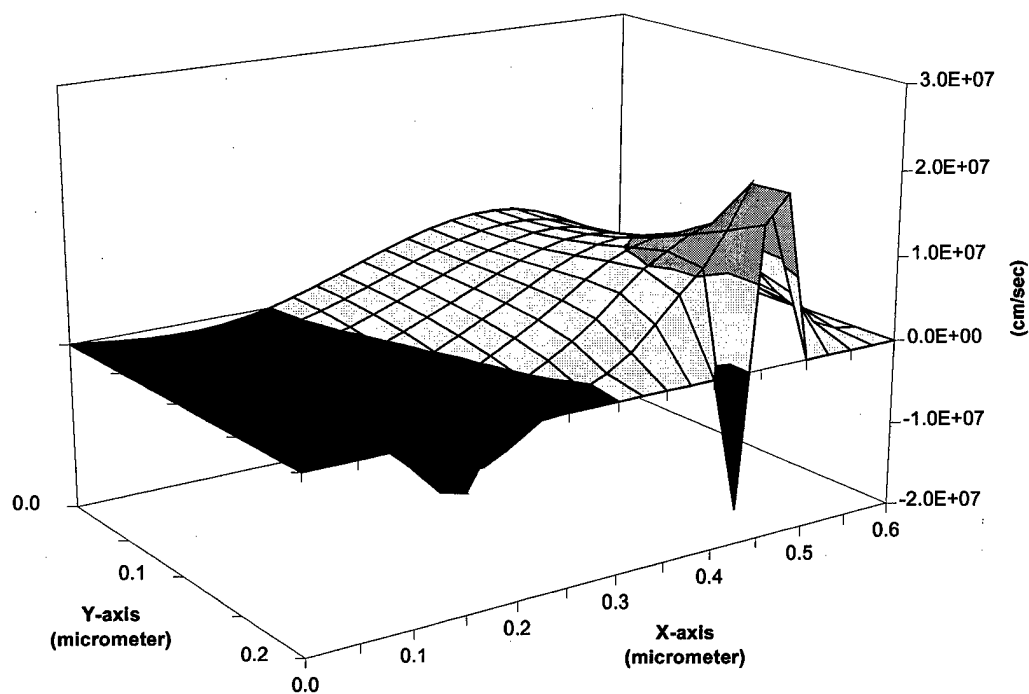


Fig. 6.15(b) Longitudinal velocity at 0.5ps.

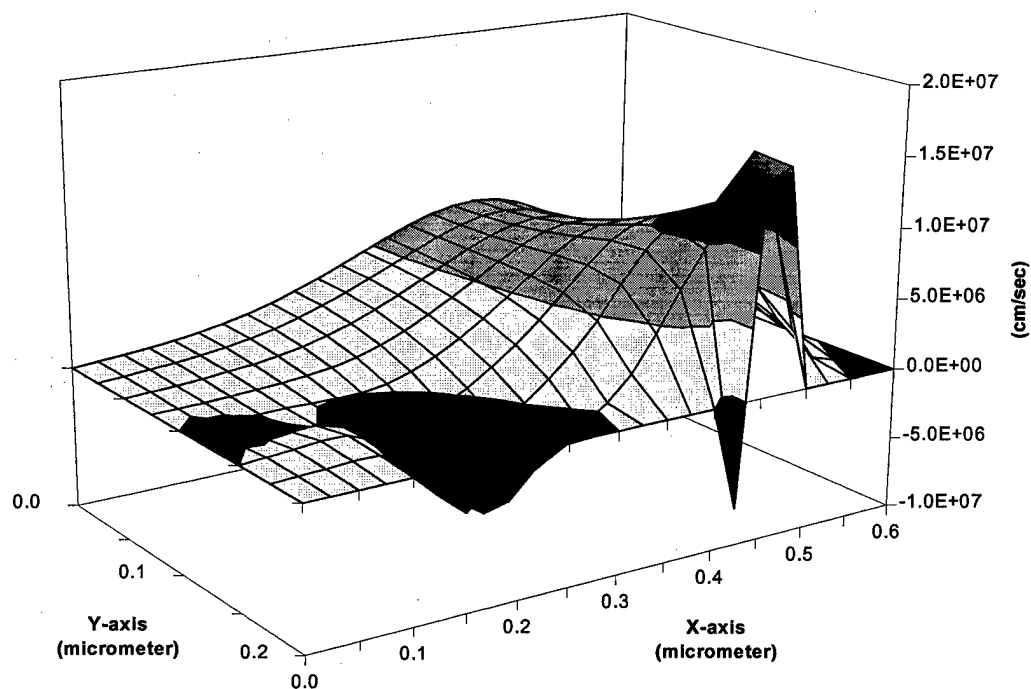


Fig. 6.15(c) Longitudinal velocity at 1ps.

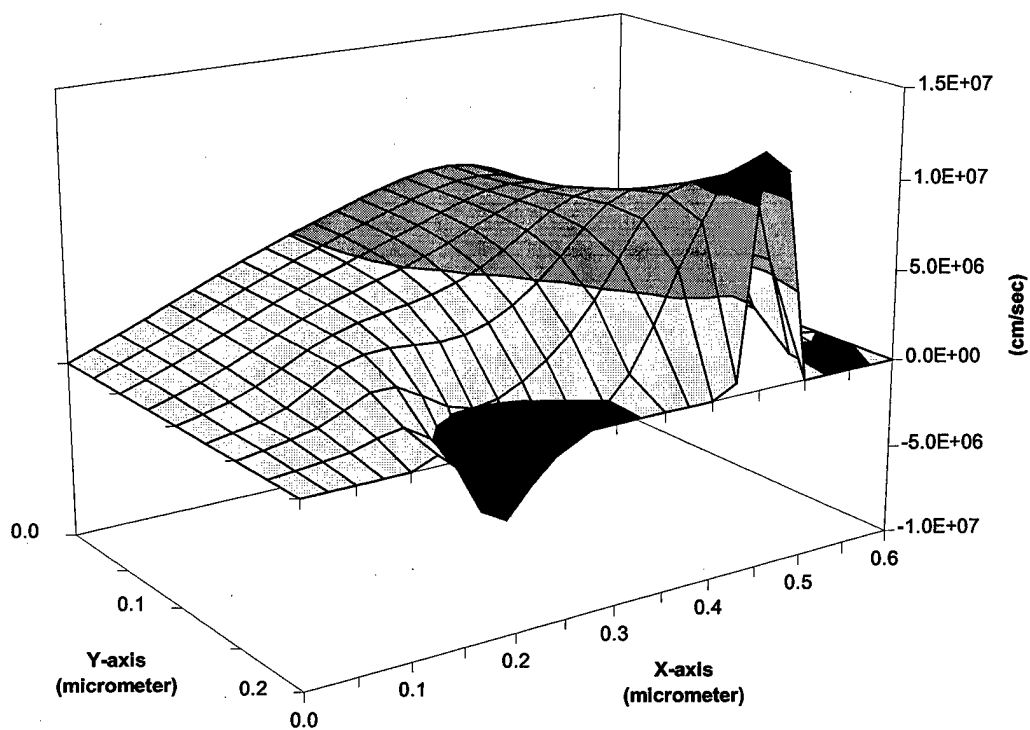


Fig. 6.15(d) Longitudinal velocity at 2ps.

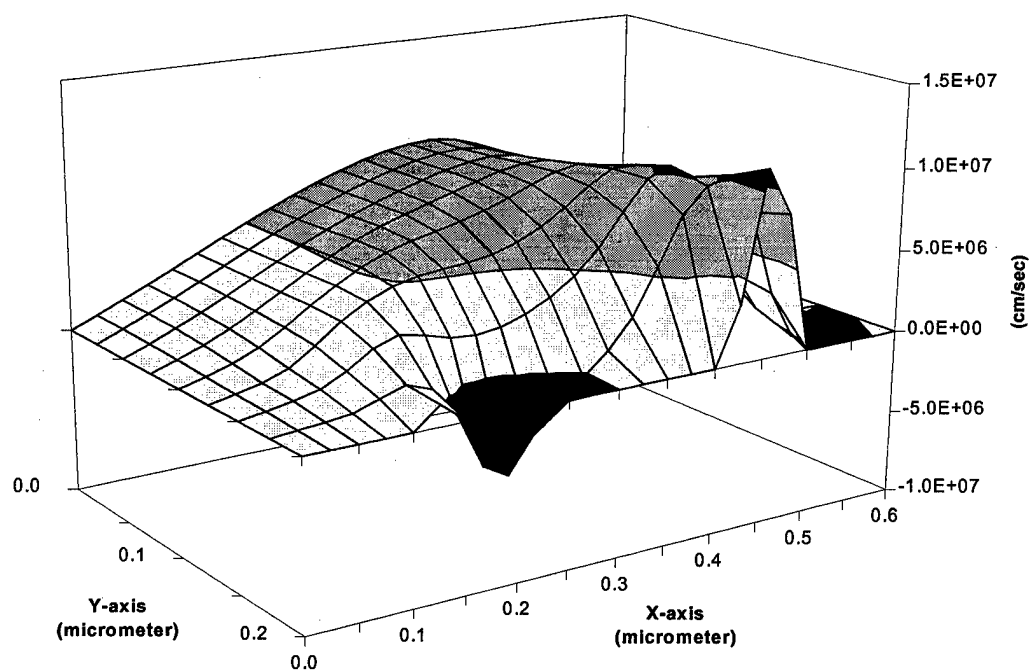


Fig. 6.15(e) Longitudinal velocity at 5.5ps.

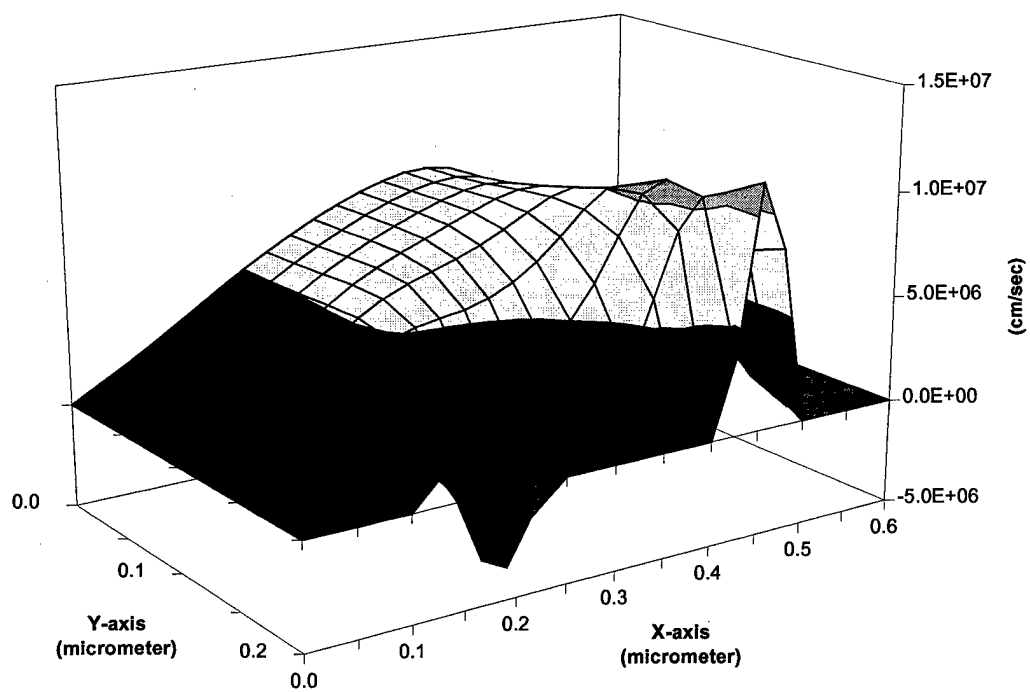


Fig. 6.15(f) Longitudinal velocity at 10ps.

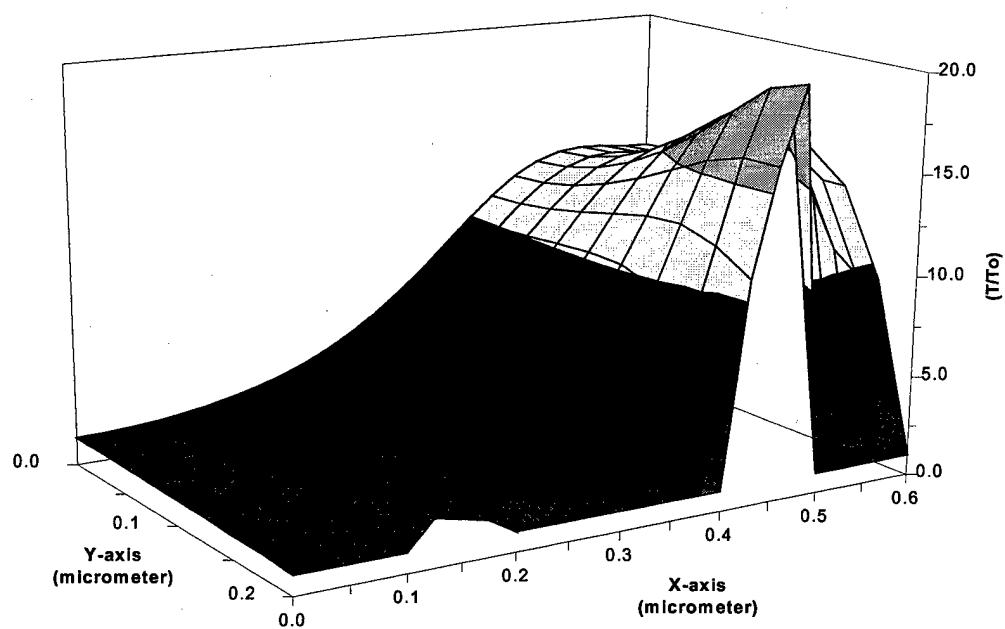


Fig. 6.16(a) Electron Temperature at 0.05ps.

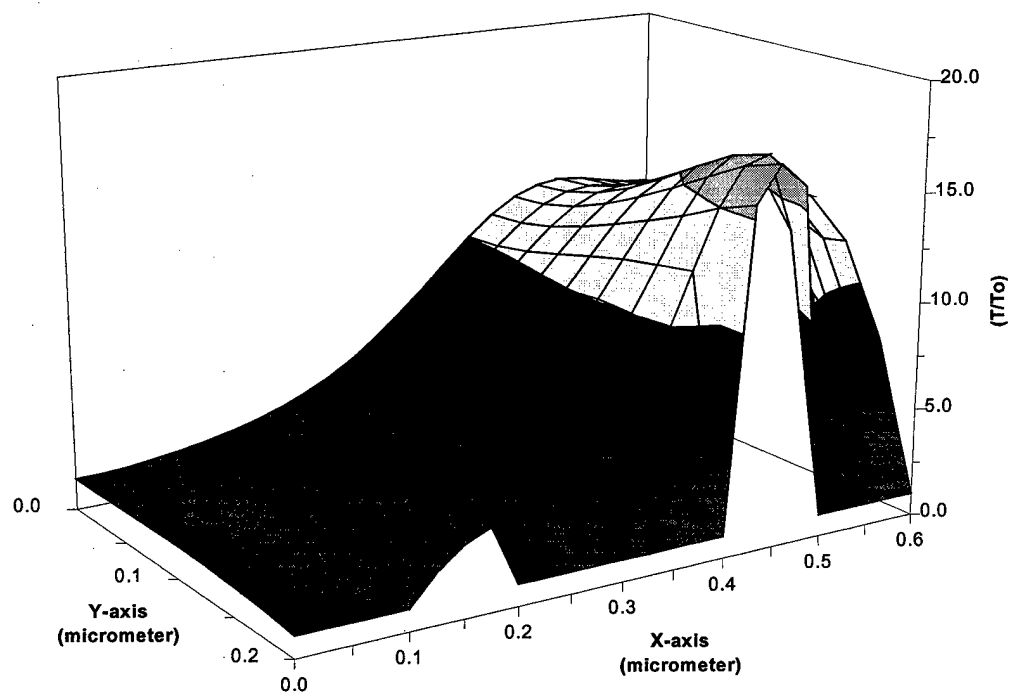


Fig. 6.16(b) Electron Temperature at 0.5ps.

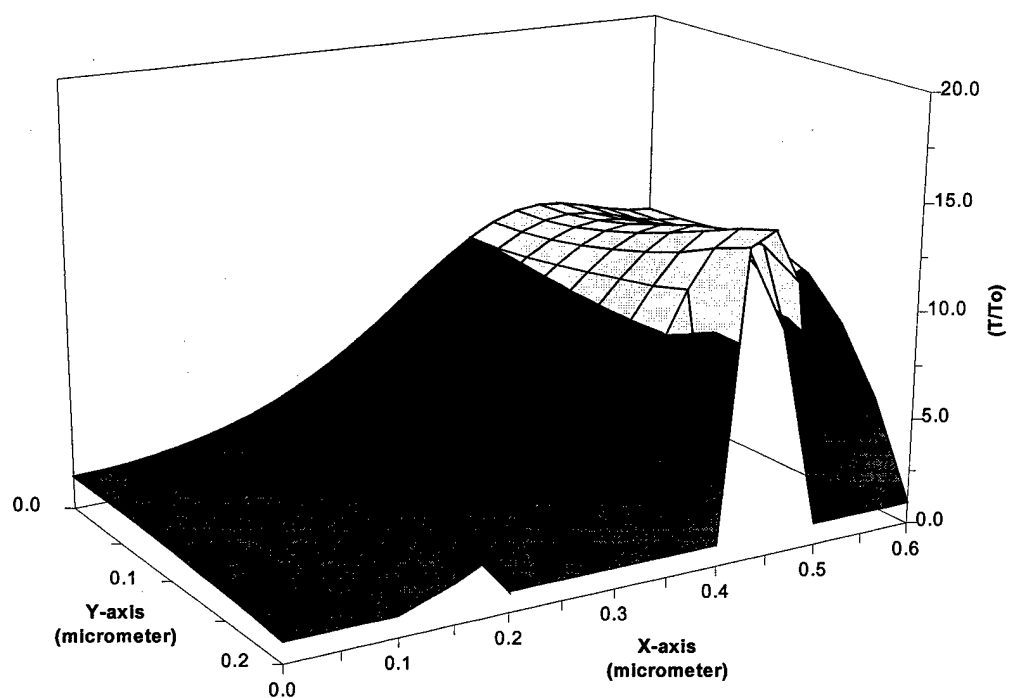


Fig. 6.16(c) Electron Temperature at 1ps.

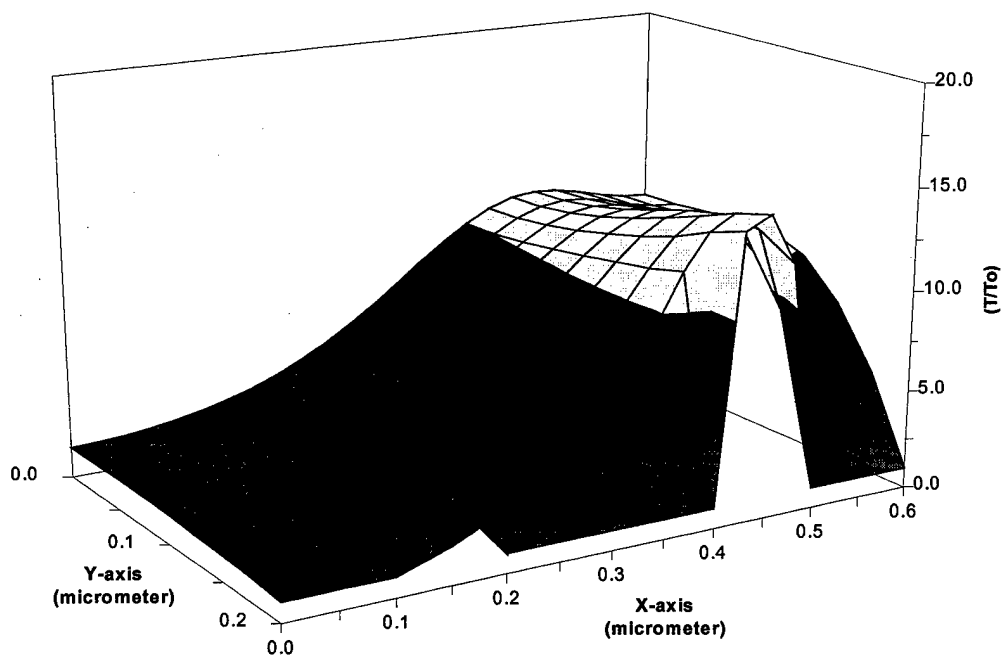


Fig. 6.16(d) Electron Temperature at 2ps.

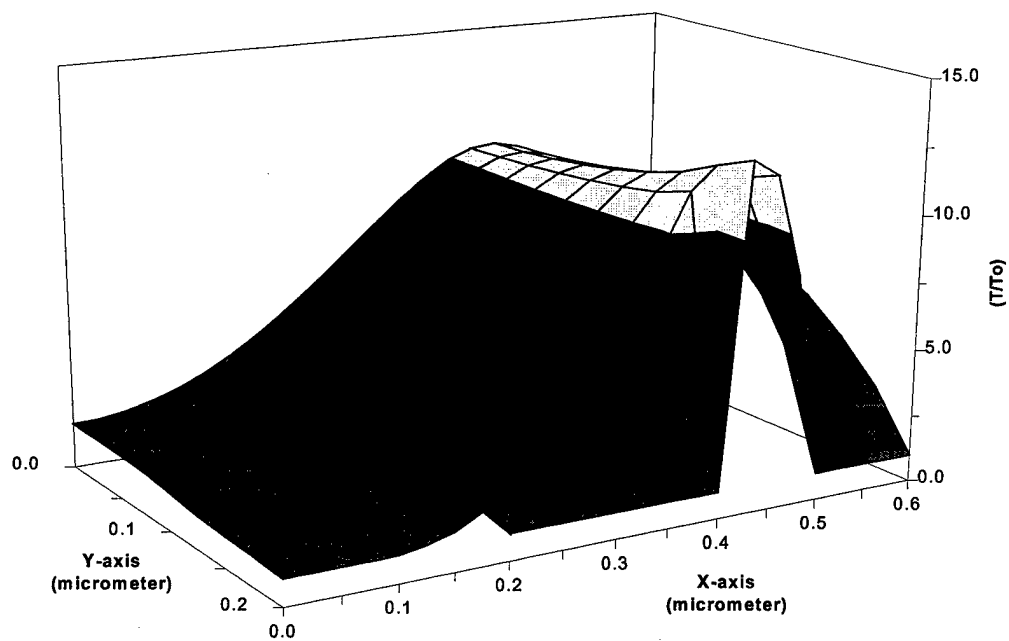


Fig. 6.16(e) Electron Temperature at 5.5ps.

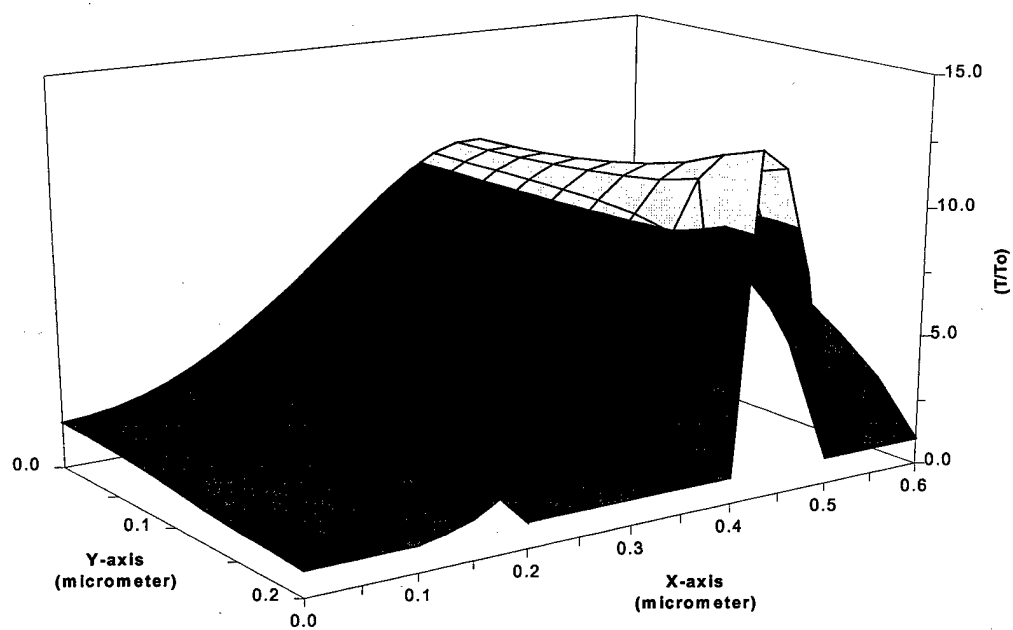


Fig. 6.16(f) Electron Temperature at 10ps.

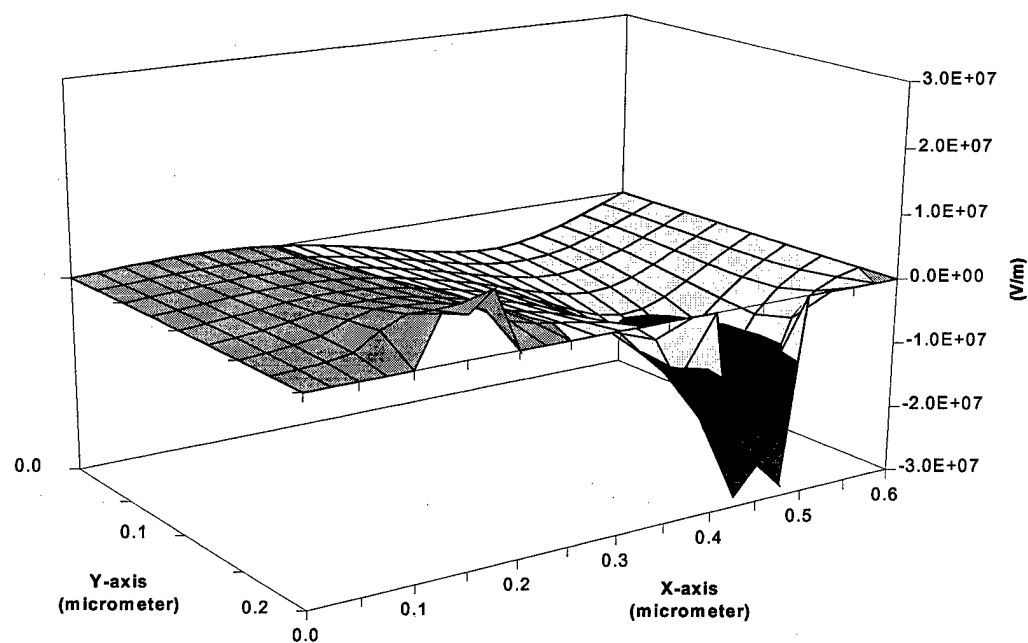


Fig. 6.17(a) Longitudinal electric field at 0.05ps.

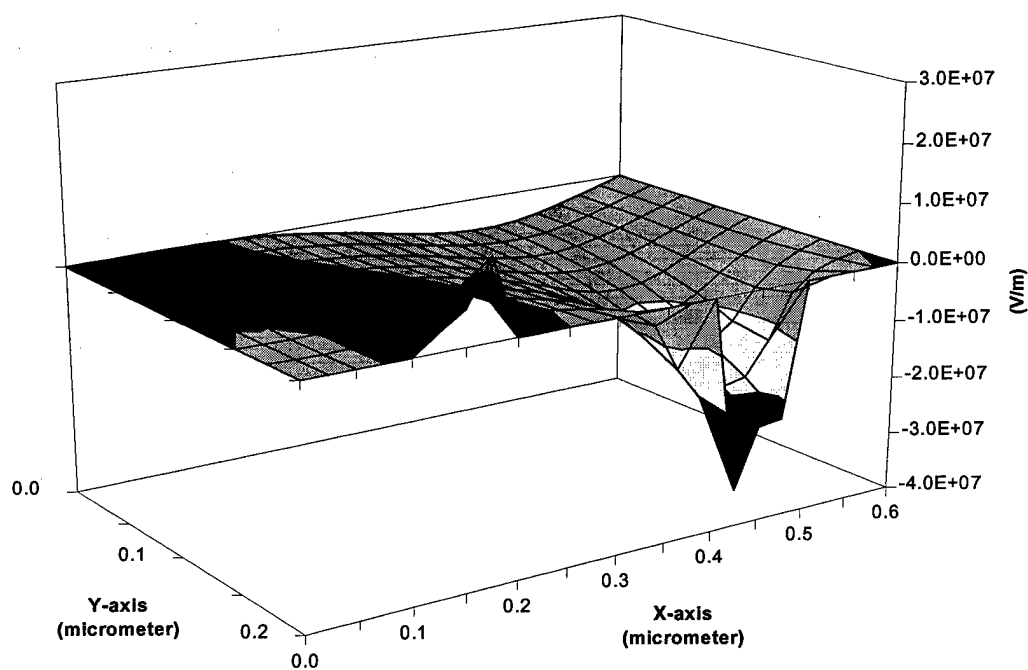


Fig. 6.17(b) Longitudinal electric field at 0.5ps.

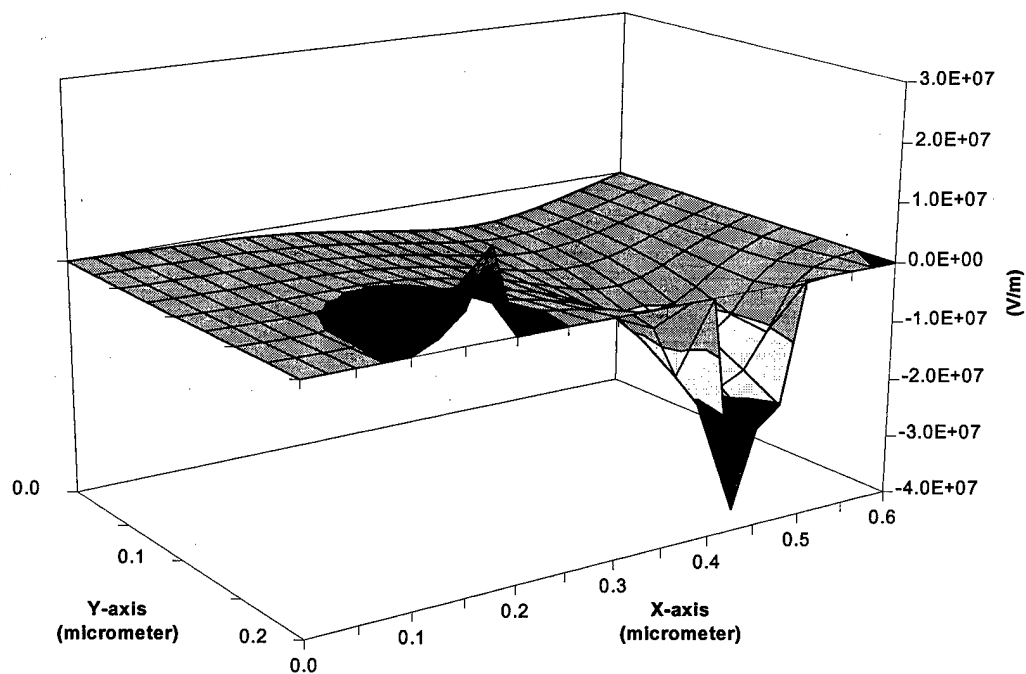


Fig. 6.17(c) Longitudinal electric field at 1ps.

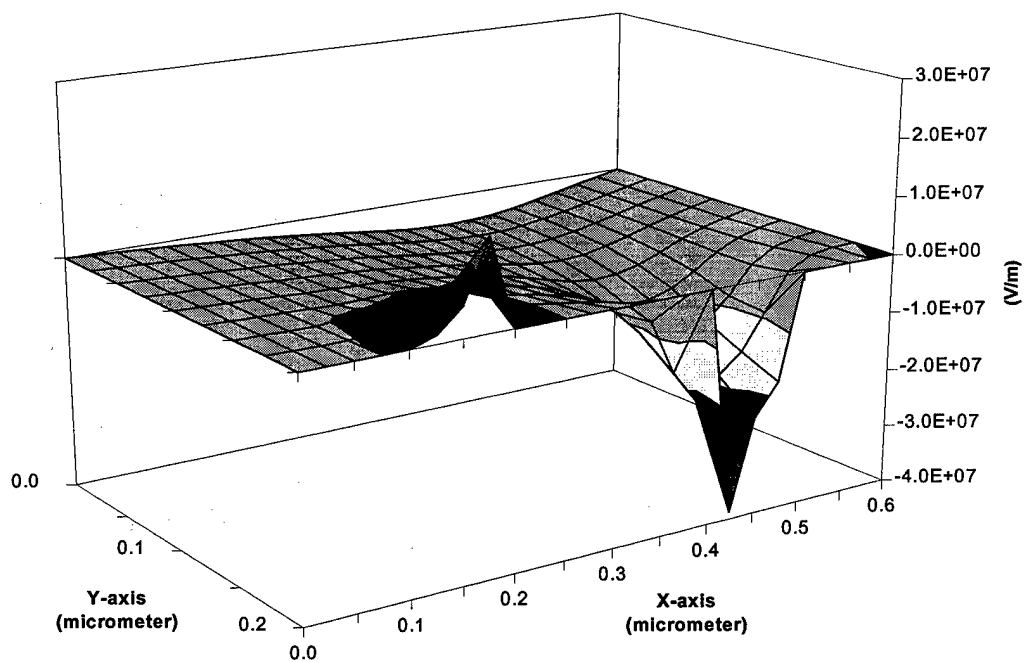


Fig. 6.17(d) Longitudinal electric field at 2ps.

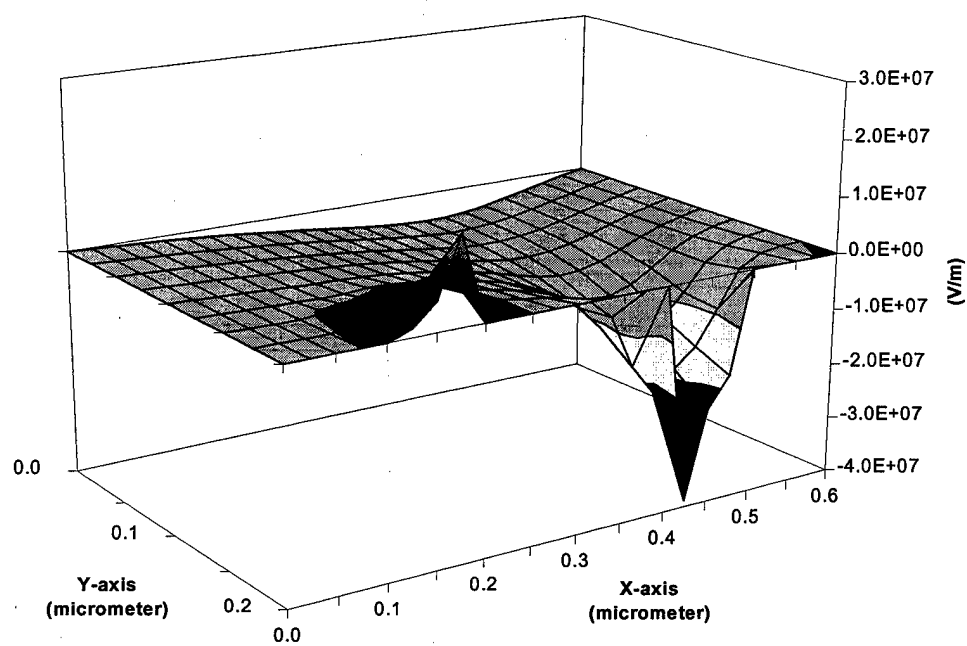


Fig. 6.17(e) Longitudinal electric field at 5.5ps.

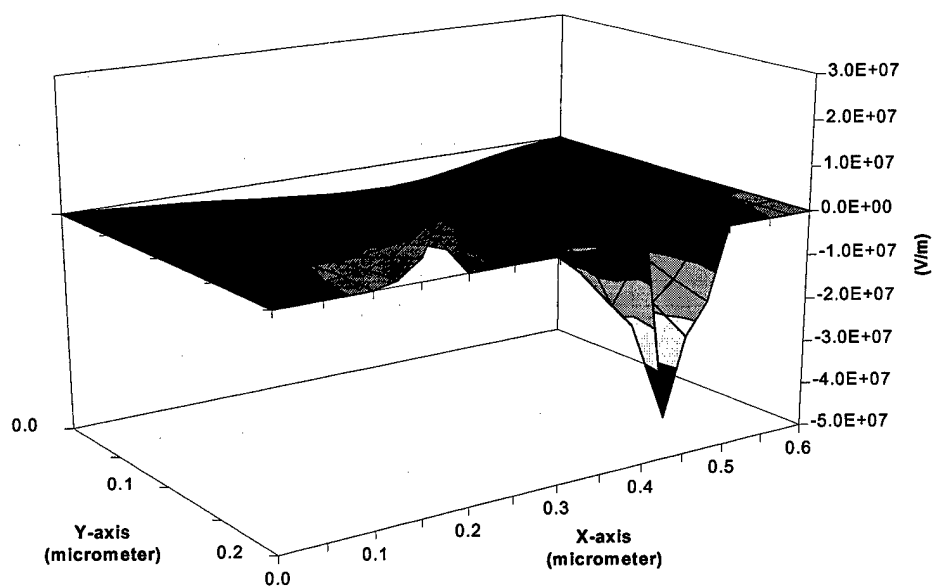


Fig. 6.17(f) Longitudinal electric field at 10ps.

6.3 Two Dimensional MOSFET

In this section, we present our simulation results of the behavior of a deep submicron n-channel silicon MOSFET. This test device is the same as the device presented in [48]. It is characterized by an oxide thickness $t_{ox}=7\text{nm}$, a junction depth $x_j=0.1\mu\text{m}$, and a substrate doping level of 10^{17}cm^{-3} . The length of the source and drain contact is $0.15\mu\text{m}$, and the doping value in the n^+ region is $2\times 10^{20}\text{cm}^{-3}$. The effective channel length is approximated $0.25\mu\text{m}$. The device structure and doping profile are shown in Fig. 6.18. A gaussian doping profile is assumed within the source and the drain diffusions. The doping profile has been shown in Fig. 6.19. This simulation was applied on a 21×20 nonuniform mesh.

The first set of our calculations were performed on the silicon MOSFET with $V_{DS}=3\text{V}$ and $V_{GS}=3\text{V}$. Fig. 6.20 shows the values of the electrostatic potential for the device. The figure reflects the large variation of the electrostatic potential occurring near the drain with respect to the source and bulk. The electron concentration and normalized electron temperature are shown in the Fig. 6.21 and 6.22, respectively. The electron temperature has a peak value around the high field region near the drain, and drops as the drain region is approached. The electron longitudinal velocity is shown in Fig. 6.23. The peak velocity is about $1.2\times 10^7\text{cm/sec}$, it is very close to the saturation velocity. Fig. 6.24 shows the drain current verse drain voltage for two different gate voltages.

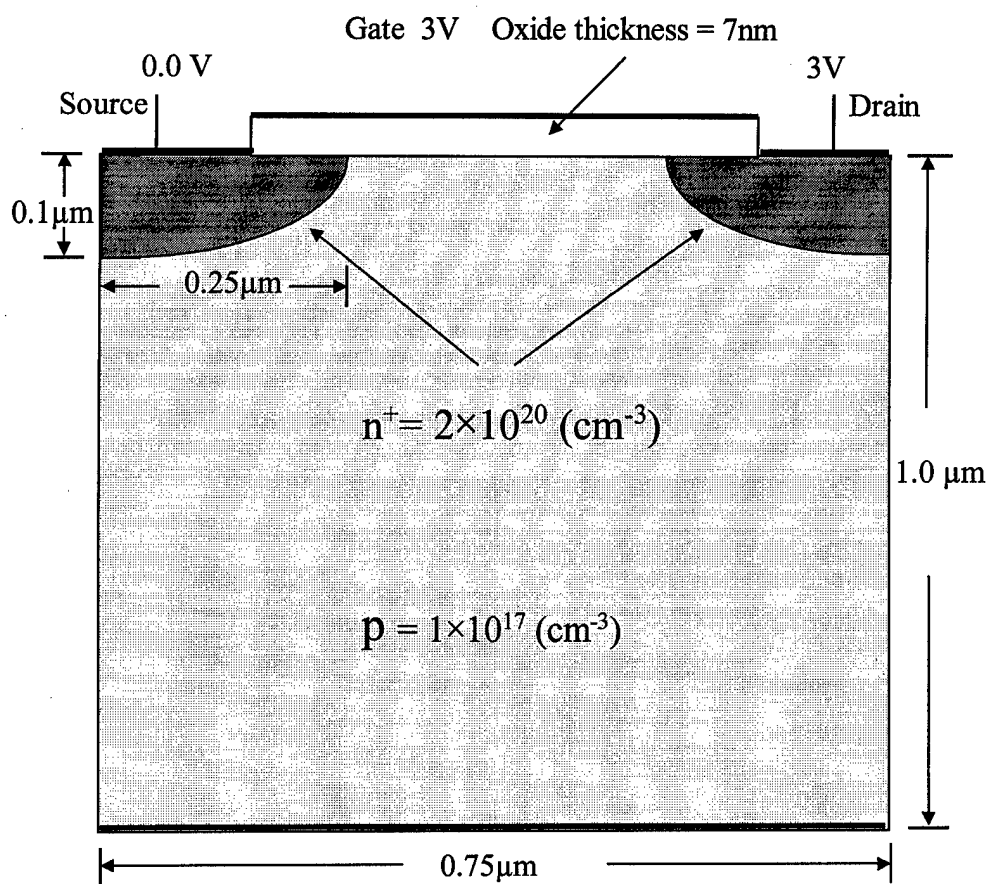


Fig. 6.18 A two-dimensional Silicon MOSFET device

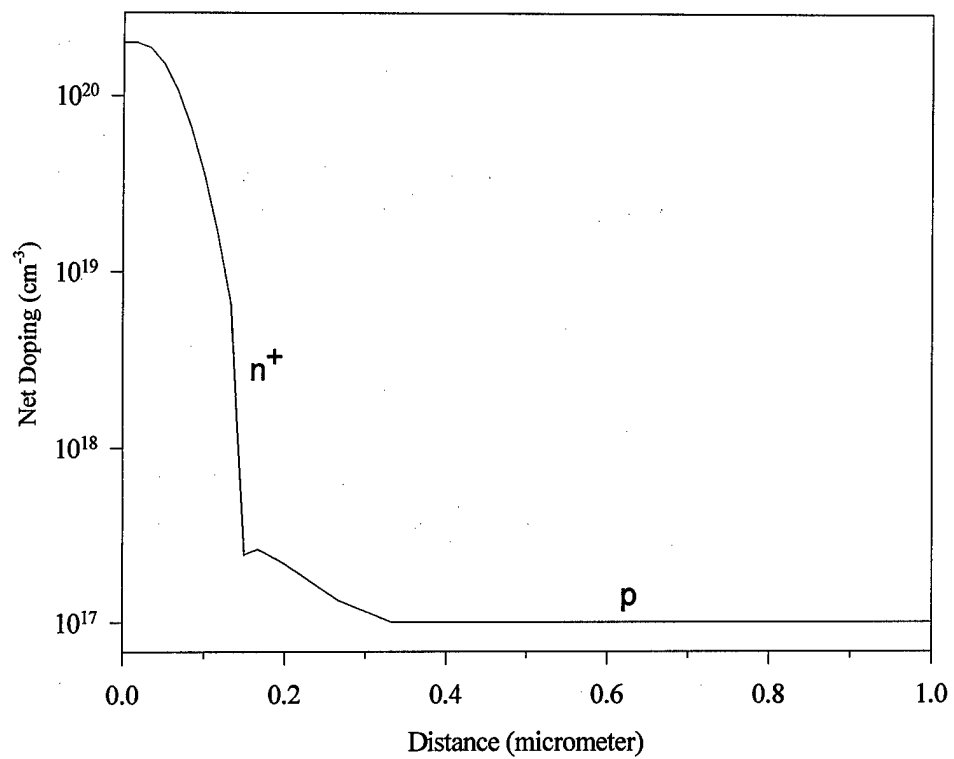


Fig. 6.19 Source and Drain impurity profile

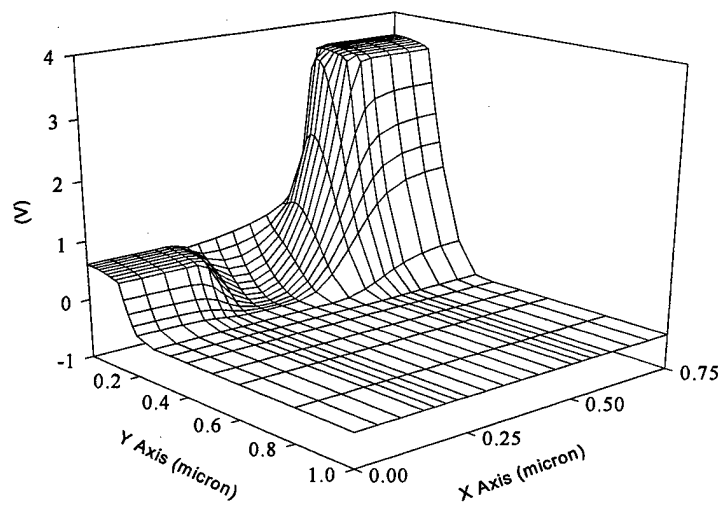


Fig. 6.20 Electrical Potential ($V_{DS}=3V, V_{GS}=3V$)

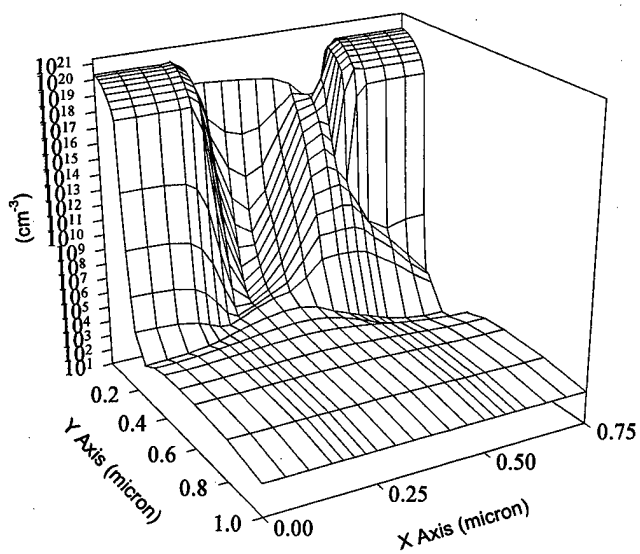


Fig. 6.21 Electron concentration ($V_{DS}=3V, V_{GS}=3V$)

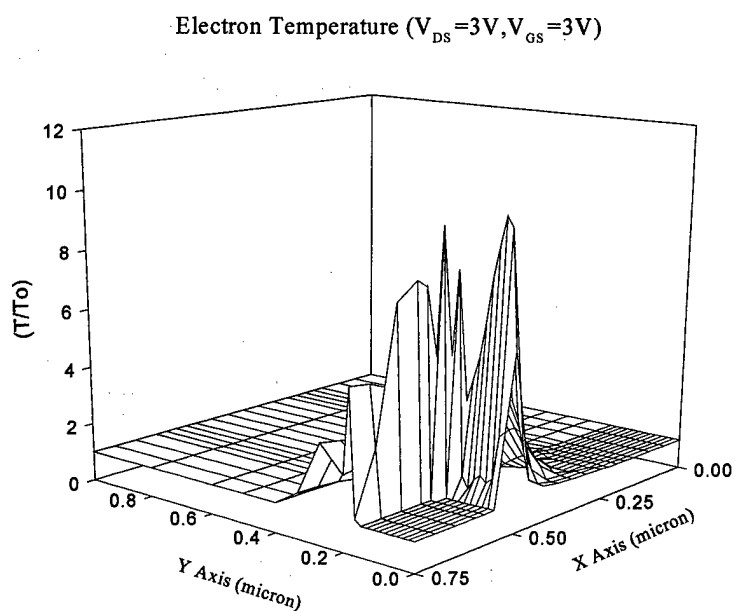


Fig. 6.22 Electron temperature ($V_{DS}=3V, V_{GS}=3V$)

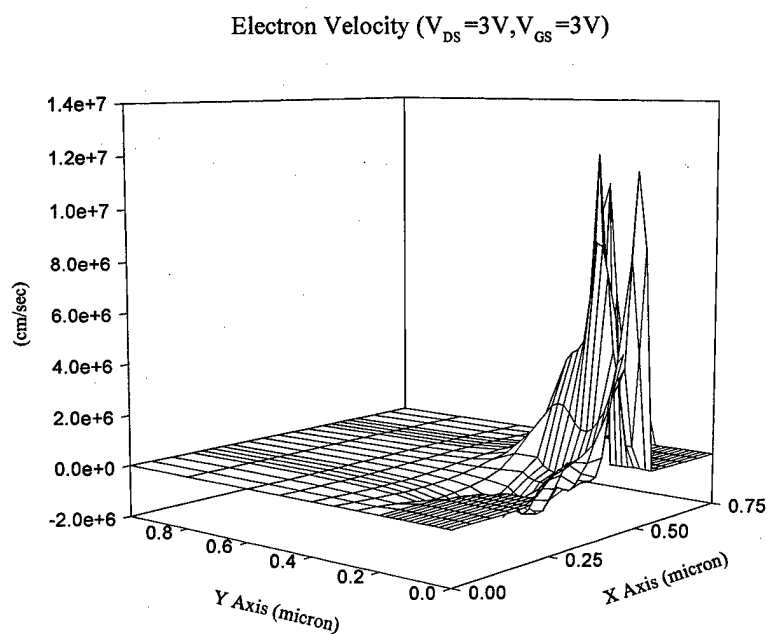


Fig. 6.23 Electron longitudinal velocity ($V_{DS}=3V, V_{GS}=3V$)

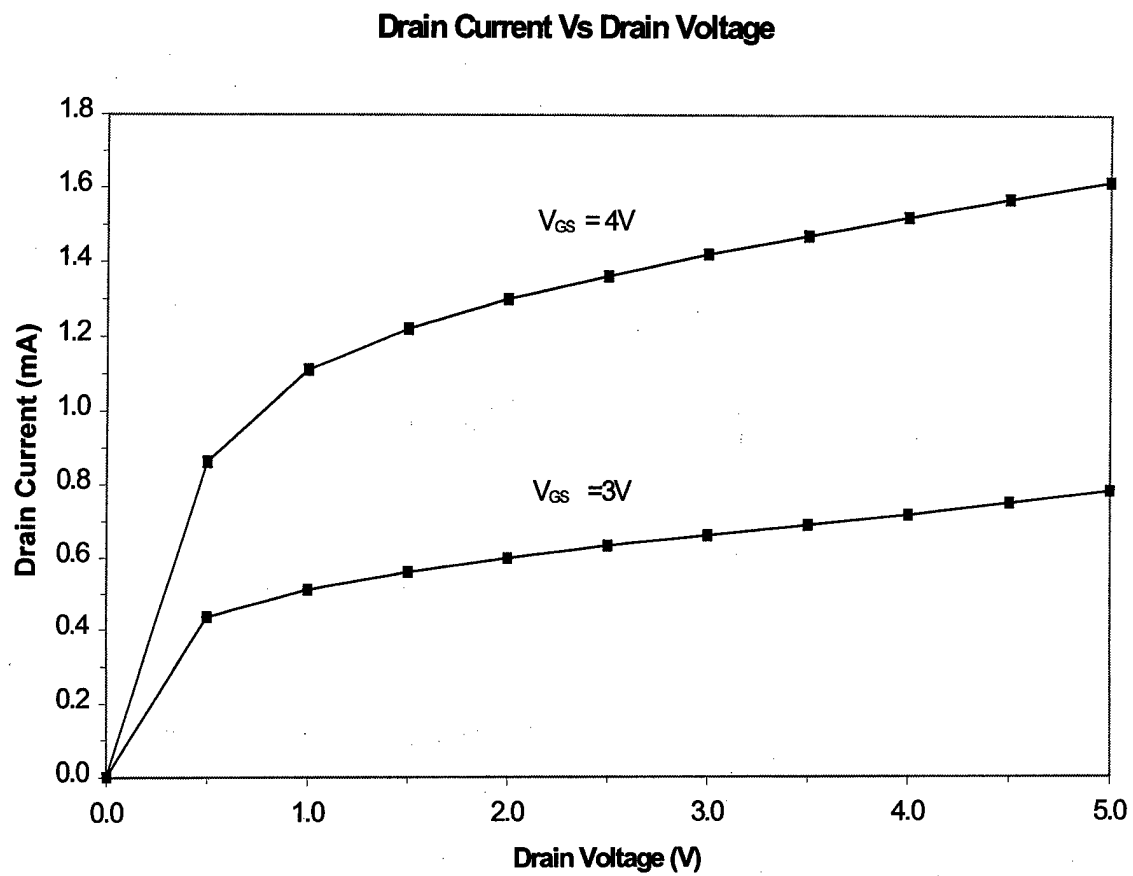


Fig. 6.24 Drain current vs. Drain voltage characteristics with indicated various gate voltage.

7. Discussion and Conclusions

In this work, a semiconductor device simulator based on the Lei-Ting hydrodynamic balance equation has been developed. The results are in general accord with other methods, such as classical hydrodynamic models and Monte Carlo models. However, our method treats scattering within the model itself, and it has the potential of including electron-electron interaction and dynamic, nonlocal screening. These quantities are calculated within the simulation process, as functions of the electron drift velocity, electron temperature, as well as the electron density, without an outside Monte Carlo procedure. Thus, besides the usual advantages of traditional hydrodynamic simulation approaches, the present method enjoys the added convenience of self-contained treatment of scattering.

We have applied our hydrodynamic balance model to n^+n-n^+ ballistic diode, MESFET and MOSFET. The numerical results demonstrate the basic hot carrier effect involving the spatial and transient velocity overshoot. We also note that the spurious overshoot peak, which usually exists in other hydrodynamic models when electric field drastically decreases, does not show in our result.

A generalized Scharfetter-Gummel discretization scheme with the Box Integration method has been employed on the numerical algorithm. Also, a new transient simulation process has been proposed and applied on the n^+n-n^+ diode and MESFET. The new algorithm has both the advantages of larger time steps compared to conventional decoupled schemes and lesser memory requirement compared to coupled scheme.

REFERENCES

1. G. Baccarani and M. R. Wordeman, "An investigation of steady-state velocity overshoot in silicon," *Solid-State Electron.*, vol. 28, no. 4, pp. 407-416, 1985.
2. R. K. Cook and J. Frey, "An efficient technique for two-dimensional simulation of velocity overshoot effects in Si and GaAs devices," *COMPEL*, vol. 1, no. 2, pp. 65-87, 1982.
3. M. Lundstrom, *Fundamentals of Carrier Transport*, Addison-Wesley, 1990.
4. K. Hess, *Advanced Theory of Semiconductor Devices*, Prentice-Hall, Englewood, NJ, 1988.
5. M. Tomizawa, K. Tokoyama, and A. Yoshi, "Nonstationary carrier dynamics in quarter-micron Si MOSFET's," *IEEE Trans. Computer-Aided Design*, vol. 7, no. 2, pp. 254-262, 1988.
6. B. Meinerzhagen and W. L. Engl, "The influence of the thermal equilibrium approximation on the accuracy of classical two-dimensional numerical modeling of silicon Submicrometer MOS transistors," *IEEE Trans. Electron Devices*, vol. 35, no. 5, pp. 689-697, 1988.
7. C. Jacoboni and L. Reggiani, "The Monte Carlo method for the solution of charge transport in semiconductors with applications to covalent materials," *Reviews of Modern Physics*, vol. 55, pp. 645-705, 1983.
8. C. Jacoboni and P. Lugli, *The Monte Carlo Method for Semiconductor Device Simulation*, Springer Verlag, Vienna, 1989.
9. K. Hess, ed., *Monte Carlo Device Simulation: Full Band and Beyond*, Kluwer Academic Publishers, 1991.
10. M. V. Fischetti, "Monte Carlo simulation of transport in technologically significant semiconductors of the diamond and zinc-blende structures-part I: Homogeneous transport," *IEEE Trans. Electron Devices*, vol. 38, No. 3, pp. 634-649, 1991.
11. M. V. Fischetti and S. E. Laux, "Monte Carlo simulation of transport in technologically significant semiconductors of the diamond and zinc-blende structures-part II: Submicron MOSFET's," *IEEE Trans. Electron Devices*, vol. 38, No. 3, pp. 650-660, 1991.
12. R. Stratton, "Diffusion of hot and cold electron in semiconductor barriers," *Phys. Rev.*, vol. 126, pp. 2002-2013, 1962.
13. K. Blotekjaer, "Transport equations for two-valley semiconductors," *IEEE Trans. Electron Devices*, vol. 17, pp. 38-47, 1970.
14. G. Baccarani and M. R. Wordeman, "An investigation of steady-state velocity overshoot in silicon," *Solid-State Electron.*, vol. 28, no. 4, pp. 407-416, 1985.
15. F. Odeh, M. Rudan and J. White, "Numerical solution of the hydrodynamic model for a one-dimensional semiconductor device," *COMPEL*, vol. 6, pp. 151-170, 1987.
16. D. Chen, E. C. Kan, U. Ravaioli, W.-C. Shu, and R. W. Dutton, "An improved energy transport model including nonparabolicity and non-Maxwellian distribution effects," *IEEE Electron Device Lett.*, vol. 13, no. 1, pp. 26-28, 1992.
17. D. L. Woolard, R. J. Trew, and M. A. Littlejohn, "Hydrodynamic hot-electron transport model with Monte-Carlo generated transport parameters," *Solid-State Electron.*, vol. 31, pp. 571-574, 1988.

18. S.-C. Lee and T.-W. Tang, "Transport coefficients for a silicon hydrodynamic model extracted from inhomogeneous Monte Carlo calculations," *Solid-State Electron.*, vol. 35, no. 4, pp.561-569, 1992.
19. X. L. Lei, J. Cai, and L. M. Xie, "High-field balance equation for electronic transport in weakly nonuniform systems," *Phys. Rev. B* vol.38, no. 2, pp.1529-1532, 1987.
20. X. L. Lei and C. S. Ting, "Green's-function approach to nonlinear electronic transport for an electron-impurity-phonon system in a strong electric field," *Phys. Rev. B* vol.32, no. 2, pp.1112-1132, 1985.
21. J. Cai and H. L. Cui, "Semiconductor device simulation with the Lei-Ting balance equations," *J. Appl. Phys.* Vol.78, No.11, 1995.
22. X. L. Lei, N. J. M. Horing, and H. L. Cui, "Theory of negative differential conductive in a superlattice miniband," *Phys. Rev. Letters* vol. 66, no. 25, pp.3277-3280, 1991.
23. X. L. Lei, N. J. M. Horing, H. L. Cui, and K.K. Thornber, "Frequency limitations of negative differential mobility in vertical conduction in superlattices," *Appl. Phys. Letters* vol. 65, no. 23, pp. 2984-2986, 1994.
24. S. Choi, J. G. Ahn, Y. J. Park, H. S. Min, and C. G. Hwang, "A time dependent hydrodynamic device simulator SNU-2D with new discretization scheme and algorithm," *IEEE Trans. Computer-Aided Design of Integrated Circuits and Systems*, vol.13, No. 7, pp.899-908, 1994.
25. M. Rudan, F. Odeh, and J. White, "Numerical solution of the hydrodynamic model for a one-dimensional semiconductor device," *COMPEL-Int. J. Comp. Math. Electrical Electron Eng.* vol. 6, no. 3, pp.151-170, 1987.
26. A. Forghieri, R. Guerrieri, P. Ciampolini, A. Gnudi, M. Rudan and G. Baccarani, "A New Discretization Strategy of the Semiconductor Equations Comprising Momentum and Energy Balance," *IEEE Trans. Computer-Aided Design*, vol. 7, pp.231-242, 1988.
27. C. C. Lee, H. L. Cui, J. Cai, E. Lenzing, R. Pastore, D. Rhodes and B. S. Perlman, "Transient device modeling using the Lei-Ting hydrodynamic balance equations," *J. Appl. Phys.*, vol. 80, no. 3, pp. 1891-1900, 1996.
28. C. C. Lee, H. L. Cui, J. Cai, R. Pastore, D. Woolard, D. Rhodes and B. S. Perlman, "Time dependent hydrodynamic model of MESFET," *Fifth International Workshop on Computational Electronics*, 1997.
29. W. Haensch and M. Miura-Mattausch, "The hot-electron problem in small semiconductor device," *J. Appl. Phys.* 60, pp. 650, 1986.
30. X. L. Lei, J. C. Cao, and B. Dong, "Study of high-field electron transport in semiconductors using balance equations for nonparabolic multivalley systems," *J. Appl. Phys.*, vol. 80, no. 3, pp. 1504-1509, 1996.
31. H. K. Gummel, "A self-consistent iterative scheme for one-dimensional steady state transistor calculations," *IEEE Trans. Electron Devices*, vol. ED-11, pp.455, 1964.
32. R. S. Varaga, *Matrix Iterative Analysis*, Englewood Cliffs, NJ: Prentice Hall, 1962.
33. D.L Scharfetter and H.K. Gummel, "Large-Signal Analysis of a Silicon Read Diode Oscillator," *IEEE Trans. Electron Device*, vol.16, No.1, pp.64-77, 1969.
34. A. Forghieri, R. Guerrieri, P. Ciampolini, A. Gnudi, M. Rudan and G. Baccarani, "A New Discretization Strategy of the Semiconductor Equations Comprising Momentum and Energy Balance," *IEEE Trans. Computer-Aided Design*, vol. 7, pp.231-242, 1988.

35. A. Leone, A. Gnudi and G. Baccarani, "Hydrodynamic simulation of semiconductor device operating at low temperature," IEEE Trans. Computer-Aided Design of integrated Circuits and Systems, vol.13, no. 11, pp.1400-1408, 1994.
36. Press, W. H., S. A. Teukolsky, W. T. Vetterling, B. P. Flannery, Numerical Recipes, Cambridge, New York: Cambridge University Press, 1987.
37. S. Yoganathan and S. K. Banerjee, "A new decoupled algorithm for nonstationary, transient simulations of GaAs MESFET's," IEEE Trans. Electron Dev. Vol.39, no. 7, pp.1578-1587, 1992.
38. M.S. Obrecht, M.I. Elmasry, "TRASIM: Compact and Efficient two-dimensional transient simulator for arbitrary planar semiconductor devices," IEEE Trans.Computer-Aided Design of Integrated Circuits and Systems, vol.14, no. 4, 1995.
39. B. S. Polsky and J. S. Rimshans, "Half-implicit difference scheme for numerical simulation of transient processes in semiconductor devices," Solid-State Electronics, vol. 29, No. 3, pp. 321-328, 1986.
40. Q. Lin, N. Goldsman and G.-C. Tai, "Highly stable and routinely convergent 2-dimensional hydrodynamic device simulation," Solid-State Electronics, vol. 37, No. 2, pp. 359-371, 1994.
41. T.-W. Tang, S. Ramaswamy, and J. Nam, "An improved hydrodynamic transport model for silicon," IEEE Trans. Electron Dev. Vol. 40, no. 8, pp.1469-1477, 1993.
42. P. Wild, "On the stability of the time discretizations for the semiconductor equations," COMPEL-Int. J. Comp. Math. Electrical Electron. Eng.vol. 10, no. 1, pp.11-25, 1991.
43. E. Fatemi, J. Jerome, and S. Osher, "Solution of the hydrodynamic device model using high-order nonoscillatory shock capturing algorithms," IEEE Trans. Computer-Aided Design, vol. 10, No. 2, pp.232-244, 1991.
44. E. D. Lyumkis, B. S. Polsky, A. I. Shur and P. Visocky, "Transient semiconductor device simulation including energy balance equation," COMPEL, vol.11, No. 2, pp. 311-325, 1992.
45. M. B. Patil and U. Ravaioli, "Transient simulation of semiconductor devices using the Monte-Carlo method," Solid-State Electronics, vol. 34, No. 10, pp 1029-1034, 1991.
46. K. Tomizawa, Numerical simulation of submicron semiconductor device, Boston: Artech House, 1993.
47. Aluru, N. R., Kincho H. Law, Peter M. Pinsky, Arthur Raefsky, Ronald J. G. Goossens, and Robert W. Dutton, "Space-Time Galerkin/Least-Squares Finite Element Formulation for the Hydrodynamic Device Equations," IEICE Trans. Electron, vol. E77-C, pp. 227-235, 1994.
48. W. Lee et al., "Numerical modeling of advanced semiconductor devices," IBM J. Res. Develop., vol. 36, No. 2, pp.208-230, 1992.